Reaction Rate Sensitivity of the Production of γ-ray Emitting Isotopes in Core-Collapse Supernova

Kirby Hermansen,[1,2,3] Sean M. Couch,[1,2,3,4] Luke F. Roberts,[1,2,3] Hendrik Schatz,[1,2,3] and MacKenzie L. Warren[2,3,5,*]

[1]*National Superconducting Cyclotron Laboratory, Michigan State University, East Lansing, MI 48824, USA*

[2]*Department of Physics and Astronomy, Michigan State University, East Lansing, MI 48824, USA*

[3]*Joint Institute for Nuclear AstrophysicsCenter for the Evolution of the Elements, Michigan State University, East Lansing, MI 48824, USA*

[4]*Department of Computational Mathematics, Science, and Engineering, Michigan State University, East Lansing, MI 48824, USA*

[5]*Department of Physics, North Carolina State University, Raleigh, NC 27695, USA*

ABSTRACT

Radioactive isotopes produced in core-collapse supernovae (CCSNe) provide useful insights into the underlying processes driving the collapse mechanism and the origins of elemental abundances. Their study generates a confluence of major physics research, including experimental measurements of nuclear reaction rates, astrophysical modeling, and γ-ray observations. Here we identify the key nuclear reaction rates to the nucleosynthesis of observable radioactive isotopes in explosive silicon-burning during CCSNe. Using the nuclear reaction network calculator *SkyNet* and current REACLIB reaction rates, we evolve temperature-density-time profiles of the innermost 0.45 $M_\odot$ ejecta from the core collapse and explosion of a 12 $M_\odot$ star. Individually varying 3403 reaction rates by factors of 100, we identify 141 reactions which cause significant differences in the isotopes of interest, namely, ^{43}K, ^{47}Ca, ^{44,47}Sc, ^{44}Ti, ^{48,51}Cr, ^{48,49}V, ^{52,53}Mn, ^{55,59}Fe, ^{56,57}Co, and ^{56,57,59}Ni. For each of these reactions, we present a novel method to extract the temperature range pertinent to the nucleosynthesis of the relevant isotope; the resulting temperatures lie within the range $T = 0.47$ to 6.15 GK. Limiting the variations to within 1σ of STARLIB reaction rate uncertainties further reduces the identified reactions to 48 key rates, which can be used to guide future experimental research. Complete results are presented in tabular form.

Keywords: Nuclear astrophysics (1129), Nucleosynthesis (1131), Core-collapse supernovae (304), Reaction rates (2081), Explosive nucleosynthesis (503), Gamma-rays (637)

1. MOTIVATION

Core collapse supernovae (CCSNe) are important nucleosynthesis sites contributing to the origin of a broad range of elements (Woosley & Weaver 1995; Rauscher et al. 2002; Woosley et al. 2002; Nomoto et al. 2006; Chieffi & Limongi 2017; Curtis et al. 2019). At the extreme conditions during the explosion, many of the synthesized nuclei are produced as radioactive isotopes. Their ultimate contribution to nucleosynthesis is determined by the first stable isotope encountered along their β- or electron capture decay chains. Most of these isotopes decay quickly, but a few have half-lives that are longer than the explosion timescale and are ejected into the interstellar medium prior to their decay. These longer-lived radioactive isotopes are of particular interest as their signatures can provide information on isotopic abundances that are difficult to obtain from spectroscopic observations

and can therefore serve as unique windows into a broad range of physics questions. These signatures include characteristic decay times of supernova light curves powered by radioactive decay, observation of characteristic γ-rays emitted in the nuclear decay by balloon or satellite based γ-ray observatories, isotopic anomalies in geological samples that incorporate supernova ejecta, or the direct detection of the ejected and subsequently accelerated radioactive isotopes as cosmic rays using space based cosmic ray observatories. Our goal here is to delineate the nuclear reactions that need to be understood to reliably predict the production of long-lived radioactive isotopes from CCSN models. This is essential for the interpretation of the observed signatures in terms of CCSN physics. We focus on isotopes produced in explosive oxygen and silicon burning, which is responsible for the synthesis of a broad range of long-lived radioactive isotopes. Explosive silicon burning is of particular interest as it occurs in the deepest layers of the supernova and can therefore provide insights into mixing and ejection mechanisms, and the delineation between ejecta and fall-back onto the compact rem-

* NSF Astronomy and Astrophysics Postdoctoral Fellow

nant, the so-called "mass-cut" (Young et al. 2006; The et al. 2006; Grebenev et al. 2012; Grefenstette et al. 2014). Other long-lived isotopes in supernovae produced by neutron capture processes in explosive carbon or helium burning layers, such as ^{41}Ca or ^{60}Fe, are not the subject of this study.

Nucleosynthesis during explosive silicon burning is governed by a typically α-rich freezeout from a quasi-statistical equilibrium (Woosley & Hoffman 1992; Hix & Thielemann 1996; Meyer et al. 1998). During quasi-statistical equilibrium groups of nuclei on the nuclear chart form equilibrium clusters, where fast nuclear reactions maintain equilibrium among the included nuclei. The resulting relative isotopic abundances within a cluster are therefore entirely determined by the thermodynamic properties of the nuclei and independent of the rates of the nuclear reactions (though the rates of the reactions determine the extent of the cluster). However, equilibrium clusters are connected by slow nuclear reactions that are critical in determining the overall abundance distribution among the clusters. As the material expands, more clusters form and more bottle-neck reactions emerge.

Sensitivity studies are needed to identify the relatively few critical bottle-neck reactions that affect the final composition. The et al. (1998) performed a sensitivity study using a simple parametrized α-rich freezeout model. They identified a number of critical reactions that affect the synthesis of ^{44}Ti by varying reactions individually by a factor of 100. A similar model was later used to identify nuclear reactions affecting the production of ^{59}Ni, ^{57}Co, ^{56}Co, and ^{55}Fe (Jordan et al. 2003). Hoffman et al. (1999) compared supernova nucleosynthesis in a full 1D explosion model of a 15 $M_\odot$ and a 20 $M_\odot$ star using two sets of reaction rates and identified the ^{40}Ca$(\alpha,\gamma)^{44}$Ti reaction rate as critical in determining the ^{44}Ti yield. Hoffman et al. (2010) used a set of parametrized expansion models to investigate the sensitivity of ^{44}Ti production in explosive silicon burning to the ^{40}Ca$(\alpha,\gamma)^{44}$Ti and ^{44}Ti$(\alpha,p)^{47}$V reaction rates over a range of possible conditions. Tur et al. (2010) explored the sensitivity of ^{44}Ti production to the ^{12}C$(\alpha,\gamma)^{16}$O reaction in three 1D supernova models based on a 15 $M_\odot$, 20 $M_\odot$, and 25 $M_\odot$ progenitor star. Magkotsios et al. (2010) carried out a full sensitivity study of the synthesis of ^{56}Ni and ^{44}Ti in explosive silicon burning using a combination of a broad set of parametrized trajectories that systematically cover the relevant parameter space, and trajectories from three supernova models: a one-dimensional CasA inspired model with a 16 $M_\odot$ star, a one-dimensional hypernova model, and a two-dimensional rotating 15 $M_\odot$ star model. They varied rates individually by factors of 100.

Here we present a much more comprehensive sensitivity study that considers all radioactive isotopes of potential interest, and uses trajectories from a self-consistent supernova simulation instead of a parametrized approach. The CCSN explosion data we use, while one-dimensional, includes the effects of convection and turbulence, accurate energy-dependent neutrino transport, and approximate general relativity. In addition, we identify for the first time the temperature range over which the model is sensitive to the reaction rate. This information is critical to guide experiments.

We begin in Section 2 by laying out the background behind detection of radioactive isotopes from CCSNe. Then, in Section 3 we describe the details of the CCSN simulation, and our post-processing calculations of nucleosynthesis using this simulation. In Section 4 we briefly summarize the results of the study, and describe several points of interest. Next, we contextualize the results in Section 5 by evaluating the significance of reactions relative to the uncertainty of their reaction rates. We also compare to past work, both in terms of the nucleosynthesis of the model and the most important reactions identified. Finally, we summarize the key differences in this work in Section 6 and conclude.

2. BACKGROUND

We now discuss the relevant radioactive isotopes and their signatures in more detail. If the half-life of a radioactive isotope produced in a CCSN is long enough to allow mixing outwards to a column depth where γ-radiation can escape, the decay γ-radiation can in principle be observed directly with balloon or satellite based γ-ray detectors (Vink 2005; Diehl 2017; Timmes et al. 2019). Such observations provide important isotopic abundance information. In addition, compared to visible light, UV, or X-rays, γ-rays are much less affected by attenuation in the surrounding gas or the interstellar medium. It is therefore much more straight forward to determine the total produced abundance, which can then be compared to CCSN model predictions. Due to the challenging instrument sensitivity requirements, only a small number of isotopes have so far been observed via their decay γ-radiation in supernova remnants. γ-rays from the decay of ^{56}Co (half-life $T_{1/2} = 77.236$ d (Tuli 2011)) were observed from supernova 1987A 160 days after the explosion by balloon experiments (Cook et al. 1988; Mahoney et al. 1988; Sandie et al. 1988; Teegarden et al. 1989) and the Solar Maximum Mission (SMM) satellite (Matz et al. 1988) (see also the review by Vink (2005)). These observations occurred prior to the expected γ-ray transparency of the ejecta, indicating the importance of mixing processes during the explosion. Later, the observation of ^{57}Co ($T_{1/2} = 271.74$ d (Tuli 2011)) decay γ-rays from 1987A with the Compton Gamma Ray Observatory (CGRO) was reported by Kurfess et al. (1992). More recently ^{44}Ti ($T_{1/2} = 60.0$ y (Tuli 2011)) was detected in 1987A via γ- and hard X-rays by INTEGRAL (Grebenev et al. 2012) and NuSTAR (Boggs et al. 2015), with total inferred amounts of ^{44}Ti of $(3.1 \pm 0.8) \times 10^{-4}$ $M_\odot$ and $(1.5 \pm 0.3) \times 10^{-4}$ $M_\odot$, respectively. For 1987A, the produced amount of ^{44}Ti can also

be inferred from the late time light curve (Jerkstrand et al. 2011; Seitenzahl et al. 2014).

The only other supernova remnant from which nuclear decay γ-rays have been unambiguously detected is Cas A, where ^{44}Ti has been detected by CGRO/COMPTEL (Iyudin et al. 1994), BeppoSAX (Vink et al. 2001), INTEGRAL (Renaud et al. 2006), and NuSTAR (Grefenstette et al. 2014). The most recent analysis from INTEGRAL obtains a ^{44}Ti mass of $(1.37 \pm 0.19) \times 10^{-4}$ $M_{\odot}$ (Siegert et al. 2015), while the result from NuSTAR is $(1.25 \pm 0.3) \times 10^{-4}$ $M_{\odot}$ (Grefenstette et al. 2014). These ^{44}Ti abundances are at least a factor of 3 higher than standard 1D supernova model predictions, which provides constraints on CCSN physics such as homogeneity and the role of multi-D effects such as bi-polar explosions (The et al. 2006; Wheeler et al. 2008; Magkotsios et al. 2010; Chieffi & Limongi 2017). No other sources of ^{44}Ti besides 1987A and CasA have been identified with certainty, though a few candidates with insufficient significance to be considered detections have been reported, e.g., GROJ0852- 4642 (Vela Junior) and G1.9+0.3 (see review by Diehl (2016)). The et al. (2006) argued that the paucity of detectable ^{44}Ti in the Galaxy is in conflict with simple assumptions about CCSN thus providing additional constraints on CCSN rates, star formation, and explosion physics. In contrast, Dufour & Kaspi (2013) found the number of supernova remnants with detectable ^{44}Ti to be consistent with current models, but posited that next generation γ-ray telescopes (Timmes et al. 2019) can be expected to identify between 8 and 21 supernova remnants based on their ^{44}Ti decay flux.

Next generation γ-ray telescopes are also expected to identify a larger number of longer-lived radioactive isotopes in addition to ^{44}Ti. Timmes et al. (2019) estimate that with such an instrument ^{48}Cr, ^{48}V, ^{52}Mn, ^{56,57}Co, ^{56,57}Ni may be detectable out to a distance of 1 Mpc, and ^{43}K, ^{44}Ti, ^{44}Sc, ^{47}Sc, ^{47}Ca, ^{51}Cr, ^{59}Fe out to a distance of 50 kpc. Many of these isotopes have half-lives of just hours to days, thus requiring rapid mixing into outer layers where γ-rays can escape.

In addition to direct detection of γ-radiation, signatures of radioactive isotopes from CCSN can be found in geological samples. The analysis of the composition of primitive meteorites provides information about the presence of radioactive isotopes in the early solar system. The main isotope of interest in the context of explosive silicon burning in core collapse supernovae is ^{53}Mn ($T_{1/2} = 3.7$ My (Tuli 2011)). Analysis of isotopic anomalies created by the presence of the ^{53}Cr decay daughter in meteorites has provided a fairly accurate value for the early solar system abundance of the ^{53}Mn/^{55}Mn ratio of $6.54 \pm 0.44 \times 10^{-6}$ (Tissot et al. 2017). CCSNe are considered the dominant source, though Type Ia supernovae may also play a role (Wasserburg et al. 2006; Côté et al. 2019).

Isotopes with half-lives in excess of 0.1 My such as ^{53}Mn accumulate in the interstellar medium, and their early solar system abundance provides a data point for this accumulation at the time and location of solar system formation. This provides unique constraints on chemical evolution probing the more recent galactic chemical history, as opposed to stable isotopes that provide an integrated sample over the age of the Galaxy (Côté et al. 2019). The early solar system abundance of ^{53}Mn also probes the circumstances and timescales of solar system formation (Lugaro et al. 2018), in particular the hypothesis of late time injection by a supernova that potentially triggered the formation of the solar system (Meyer & Clayton 2000; Wasserburg et al. 2006). With this hypothesis, and using standard spherical CCSN models, there is an overproduction issue of about three orders of magnitude for ^{53}Mn and ^{60}Fe (Meyer & Clayton 2000; Wasserburg et al. 2006; Lugaro et al. 2018; Banerjee et al. 2016). This has been used to place constraints on the nature of the responsible supernova, e.g. on the layers ejected (Meyer & Clayton 2000), the nature of fallback (Takigawa et al. 2008), the mass of the progenitor (Banerjee et al. 2016), or the supernova explosion mechanism (Sawada & Maeda 2019). This underlines the importance of understanding the nuclear production processes.

Isotopic signatures of shorter-lived isotopes in supernova ejecta can also be incorporated in geological samples via presolar grains. These grains form as SiC dust in the supernova explosion and are then transported through space and incorporated in the solar system, where they can be found in primitive meteorites. Indeed, enhanced ^{44}Ca from the decay of ^{44}Ti has been found in SiC X-grains thought to originate from CCSNe (Hoppe et al. 1996; Nittler et al. 1996; Clayton 2011), see also the recent review by Nittler & Ciesla (2016). This provides not only constraints on the supernova, but also on the grain formation process.

CCSN signatures of long-lived radioactive isotopes that decay by electron capture can in principle also be identified in the composition of cosmic rays above Earth's atmosphere. After acceleration, the radioactive nuclei are fully stripped of electrons, which prevents electron capture decay and leaves the typically very weak β^+ decay branches as the only option for decay. As a result the nuclei become sufficiently stable to propagate through the interstellar medium and be detected above Earth's atmosphere (DuVernois 1997; Wiedenbeck et al. 1999; Neronov & Meynet 2016; Benyamin & Shaviv 2018). The cosmic ray source composition of radioactive isotopes inferred from such observations can therefore serve as a chronometer of the acceleration process. However, the observed composition has to be corrected for secondary production during propagation. Isotopes of interest are ^{44}Ti, ^{49}V, ^{51}Cr, ^{55}Fe, ^{57}Co, and ^{59}Ni (Benyamin & Shaviv 2018) as well as ^{53}Mn (DuVernois 1997). The upper limit on the ^{59}Ni source abundance obtained from observations with the CRIS instrument on board the Advanced Compton Explorer Space-

craft has placed constraints on cosmic ray acceleration models (Israel et al. 2005). However, Neronov & Meynet (2016) recently pointed out the critical importance of understanding the production of ^{59}Ni in explosive silicon burning for discriminating between fast and delayed cosmic ray acceleration models. A signature of ^{44}Ti in cosmic rays has been reported from CRIS (Scott 2005) and has been used to place constraints on ^{44}Ti synthesis in CCSN (Benyamin & Shaviv 2018). Finally, source limits on ^{53}Mn have been obtained from data of the Ulysses High Energy Telescope (HET) but uncertainties were too large to draw conclusions (DuVernois 1997). In addition to the detection of the above isotopes by cosmic rays, Leising (2001) estimated the X-rays produced following electron capture are detectable by the current generation of X-ray spectrometers. While not as penetrating, these X-rays provides a useful complement to γ-rays, as in the detection of ^{44}Ti in G1.9+0.3 (Borkowski et al. 2010) and the upper limit of ^{55}Fe in 1987A (Leising 2006).

In summary, understanding the production of radioactive ^{43}K, ^{47}Ca, ^{44,47}Sc, ^{44}Ti, ^{48,51}Cr, ^{48,49}V, ^{52,53}Mn, ^{55,59}Fe, ^{56,57}Co, and ^{56,57,59}Ni in CCSNe is important for the interpretation of past and future observations in terms of a broad range of CCSN physics, chemical evolution, and cosmic ray acceleration. The goal of the remainder of the paper is to identify the important nuclear reactions that need to be understood to make reliable predictions for the production of these isotopes during explosive silicon burning.

3. METHODS

3.1. Supernova Model

We use thermodynamic trajectory data from a self-consistent Supernova Turbulence In Reduced-dimensionality (STIR) explosion model of Couch et al. (2020) for a 12 $M_\odot$ progenitor star from Sukhbold et al. (2016). The STIR model includes energy-dependent, two-moment neutrino transport in the "M1" approximation (O'Connor 2015), a microphysical equation of state for dense matter (Steiner et al. 2013), and approximate general relativistic gravity (Marek et al. 2006). Total energy is approximately conserved within the STIR model when accounting for diffusive mixing of energy and composition due to turbulent convection, as discussed in Couch et al. (2020); Warren et al. (2019). The 1D explosion is achieved by a novel model for including the effects of convection and turbulence based on a Reynolds-decomposition of the hydrodynamic evolution equations which is then closed using the mixing length theory (Couch et al. 2020). The explosion model we use here for a 12 $M_\odot$ star results in a diagnostic explosion energy of 3.7×10^{50} erg and a final baryonic proto-neutron star mass (i.e., mass cut) of 1.48 $M_\odot$. In STIR, both the explosion energy and proto-neutron star mass are predictions of the model, given a progenitor structure, and are not set by hand.

The nucleosynthesis is calculated using a post-processing approximation. Temperature (T), density (ρ), electron neutrino (ν_e) flux, and electron anti-neutrino ($\bar{\nu}_e$) flux as functions of time (referred to as trajectories) are taken from 100 equal mass (4.537×10^{-3} $M_\odot$ each) zones. These zones subdivide a range in stellar radius from 1.486 $M_\odot$ to 1.935 $M_\odot$ enclosed mass, comprising the silicon and oxygen shells of the progenitor as shown in Figure 1. Figure 2 shows the thermodynamic characteristics of the trajectories using the following parameter definition for each trajectory: the peak temperature is the maximum temperature in GK, the total entropy is the entropy at peak temperature, which is nearly constant during the expansion, the peak radiation entropy is defined by Witti et al. (1994) as

$$S_{\rm rad}(T_{9,\rm peak}) = 3.33 \frac{T_{9,\rm peak}^3}{\rho_5(T_{9,\rm peak})} \tag{1}$$

where $\rho_5 = 10^{-5} \times \rho$ g cm^{-3} with entropy in units of Boltzmann constant per baryon, and the peak density is the density at peak temperature in g cm^{-3}. While the definition of peak radiation entropy assumes an ultra-relativistic electron-positron gas, the calculations in *SkyNet* assume the gas is arbitrarily relativistic and degenerate. Additionally, the innermost trajectory has a neutron excess $\eta = 1 - 2Y_e = -0.015$ while all other trajectories are in the range $0.000 < \eta \leq 0.002$. Together these trajectories span an α-rich freezeout parameter space similar to recent studies (Magkotsios et al. 2010; Hoffman et al. 2010; Vance et al. 2020).

The region we consider is located just above the mass cut. Material closer to the star is assumed to fall back onto the compact remnant, while material at larger distances does not undergo sufficient shock heating to produce the medium mass $A = 40$-60 nuclei of interest here. Since the supernova simulation ends at 1.93 s after bounce, the continuing evolution of the trajectories is modeled on an homologous expansion—the density scales as $\rho(t) = \rho_f t_f^3/t^3$, and the temperature uses the self-heating evolution described in Lippuner & Roberts (2017). We end the trajectories at 140 s after bounce, at which time all zones have cooled below 0.01 GK and no further nucleosynthesis occurs.

3.2. Nuclear Reaction Network

For each of the 100 trajectories the nucleosynthesis and final composition are calculated using the nuclear reaction network library *SkyNet* (Lippuner & Roberts 2017). The network used here includes 1683 nuclides with element numbers $Z \leq 50$ and neutron numbers $N \leq 70$ connected by 22891 total reactions. Reactions considered include heavy ion fusion reactions; proton, neutron, and α-induced reactions and their inverse; as well as β-decays, electron capture, and free nucleon-neutrino interactions. As a baseline set of nuclear reaction rates we use REACLIB v2.2 (Cyburt et al. 2010) and,
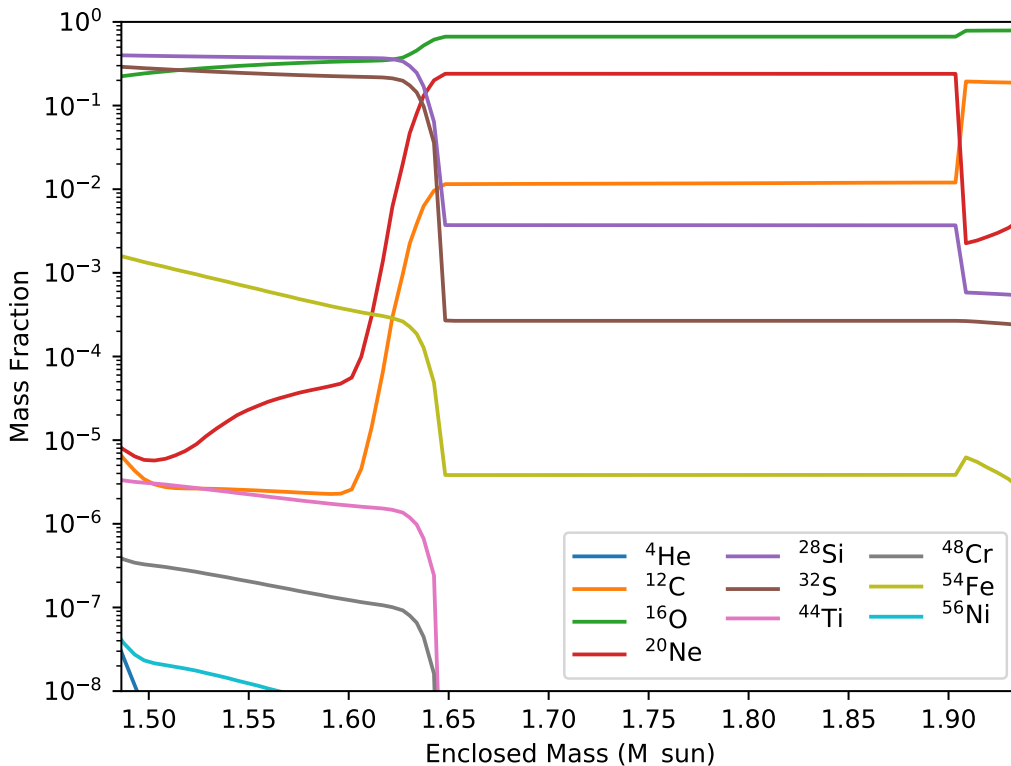
Figure 1. Initial composition of notable isotopes of the 12 $M_\odot$ star before core-collapse. Only the simulated region of enclosed mass is shown.

where available, the weak reaction rates from Langanke & Martínez-Pinedo (2000); Oda et al. (1994); and Fuller et al. (1985) as compiled by Paxton et al. (2015). Free nucleon-neutrino interactions are included as described in Lippuner & Roberts (2017) and include weak magnetism and recoil corrections from Burrows et al. (2006), consistent with the rates used in the original CCSN simulation.

The initial composition of a trajectory is taken from the same 12 $M_\odot$ progenitor model used for the supernova simulation (Sukhbold et al. 2016) (see Figure 1). The total ejected mass of an isotope of interest is determined by summing the contributions from all trajectories.

The sensitivity of the produced abundance of an isotope of interest to nuclear reaction rates is determined by changing individual reaction rates one-by-one and re-calculating the nucleosynthesis for all trajectories (Iliadis et al. 2002). To reduce the number of reactions that need to be varied, we determined a subset of relevant reactions using the calculation with the baseline rates. Only reactions with a time integrated reaction flow above 10^{-10} in any trajectory were added to the list of varied reactions. Smaller reaction flows are negligible even when varying a reaction rate by a factor as large as 100 as the smallest isotopic abundances of interest are $\approx 10^{-8}$. This approach results in a subset of 3403 relevant reactions.

Each of these reactions were individually varied up and down by factors of 100. To explore the linearity of the resulting abundance changes, we perform additional calculations for the 141 rates that significantly affect the synthesis of an isotope of interest, using smaller variations of factors of 10 and 2. In total, 737,100 network evolutions were performed.

One goal of this work is to provide guidance for nuclear physics to improve the accuracy of nuclear reaction rates that affect the nucleosynthesis of isotopes of interest. For both experimental and theoretical nuclear physics work, it is critical to understand the temperature range over which a particular reaction rate needs to be determined. We developed an approach to obtain this information for each reaction rate that was identified to affect a specific isotope i. We take advantage of the fact that reaction rates only matter during the cooling of a trajectory once Nuclear Statistical Equilibrium (NSE) breaks down. At this late stage, in our model, the temperature is monotonically decreasing. Starting with the innermost and hottest trajectory, we sum together isotopic abundances from all trajectories with $T_{\mathrm{peak}} \geq T$ until we include all simulated trajectories. We can therefore uniquely determine at each temperature T the sum of the abundances of the mass chain of isotope i ($Y_i(T)$) over all zones contributing $\geq 1\%$ to the total final abundance of that mass chain and calculate the
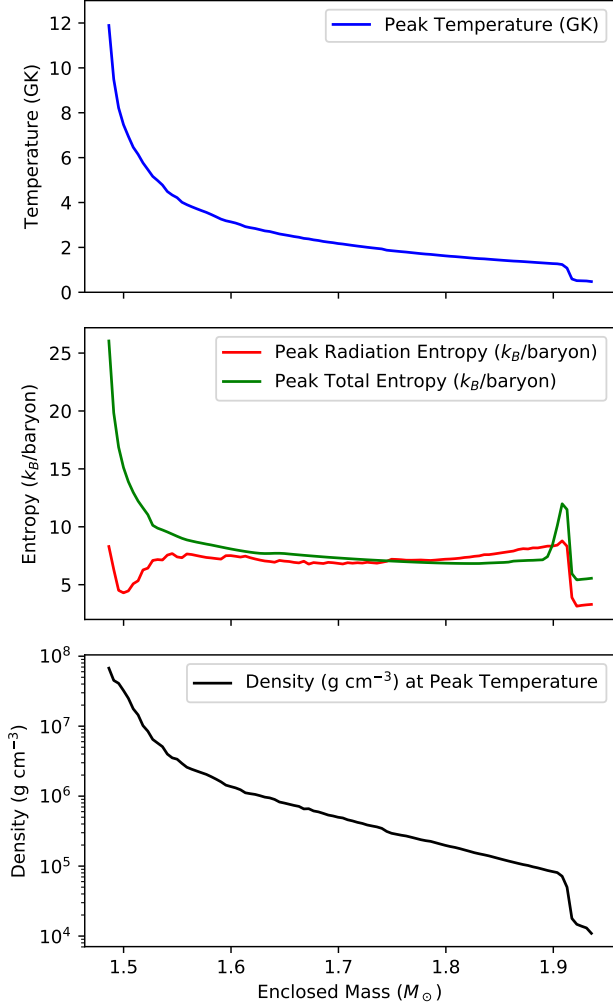
Figure 2. Thermodynamic conditions for the simulated trajectories. Peak temperature (top), peak total and peak radiation entropy (middle), and peak density (bottom). For some trajectories, peak radiation entropy is larger than peak total entropy, this is due to approximations used in the definition of peak radiation entropy.

ratio of the abundances obtained with the varied reaction rate ($Y_i'(T)$) to the baseline abundances,

$$R_i(T) = Y_i'(T)/Y_i(T) \qquad (2)$$

Figure 4 presents an example for the specific effect of varying ^{44}Ti$(\alpha,$p$)^{47}$V by x0.01 on $A = 44$ production. The sharp increases in mass chain abundance at specific, high temperatures are due to additional trajectories being included as the temperature drops. At high $T > 6.5$ GK, $R_i(T) = 1$ because abundances in NSE are insensitive to reaction rate changes. As the temperature drops, at some point R_i starts deviating from 1 and transitions to the final value, $R_{f,i}$, at low temperatures when reactions freeze out completely. We determine the temperature range $[T_{\min}, T_{\max}]$ for

the reaction rate sensitivity as the highest temperature where $\left|\log_{10} R_i(T_{\max})\right| \geq 10\% \left|\log_{10} R_{f,i}\right|$ and the lowest temperature where $\left|\log_{10} R_i(T_{\min})\right| \leq 90\% \left|\log_{10} R_{f,i}\right|$. We ignore high temperature deviations of R_i from 1 so long as R_i returns to 1 for a sustained span of 0.05 GK.

We emphasize that this is an approximate approach that makes a number of assumptions that are reasonable for this particular scenario. Most importantly we assume that temperature is dropping monotonically and that reaction rates continually become slower. The approach would not be appropriate for a scenario where some intermediate abundance is built up at one temperature, and is then processed further at another temperature (our method would only identify the second temperature range). The use of ratios instead of absolute abundances ensures that we are sensitive to reactions that change the abundance of the entire relevant equilibrium cluster even at times where the particular isotope of interest may not be fully populated within the cluster equilibrium. Also this method primarily narrows down the relevant temperature range, excluding sensitivity for higher and lower temperatures. Sensitivity within the given temperature range may not be evenly distributed.

$[T_{\min}, T_{\max}]$ then defines the temperature range over which the reaction rate has to be determined. This temperature range sensitively depends, even for the same reaction, on the isotope of interest.

4. RESULTS

Defining an impact factor,

$$F_i = 10^{\left|\log_{10} R_{f,i}\right|} \qquad (3)$$

reaction rate variations that result in final abundance changes of $F_i \geq 1.1$ (effectively a 10% difference) in an isotope of interest, i, are listed in Table 1 (moved to end for readability). Reactions are sorted by the mass number of the produced isotope of interest, and then in reverse order of impact defined as the maximum of F_i for the x100 and x0.01 variations. Final abundances for the long-lived isotopes of interest, $Y_{f,i}$, were calculated by adding the abundances of parent isotopes that had not fully decayed yet at the end of the calculation. Decays of the isotopes of interest are negligible within the 140 s of calculation time due to the much longer half-lives. For ^{48}V, ^{56}Co, and ^{57}Co the parent isotopes are also long-lived isotopes of interest. In all three cases, these isotopes are predominantly produced by the decay of their parent isotope, with direct production being negligible at 0.1%, < 0.01%, and 0.3%, respectively. The reaction rate sensitivity of the parent abundance is therefore the same as the sensitivity for the daughter abundance.

In total we find 141 reaction rates with $F_i \geq 1.1$ when varied by up to a factor of 100 for at least one isotope of interest i. The sensitivity of the final abundances to reaction rate vari-
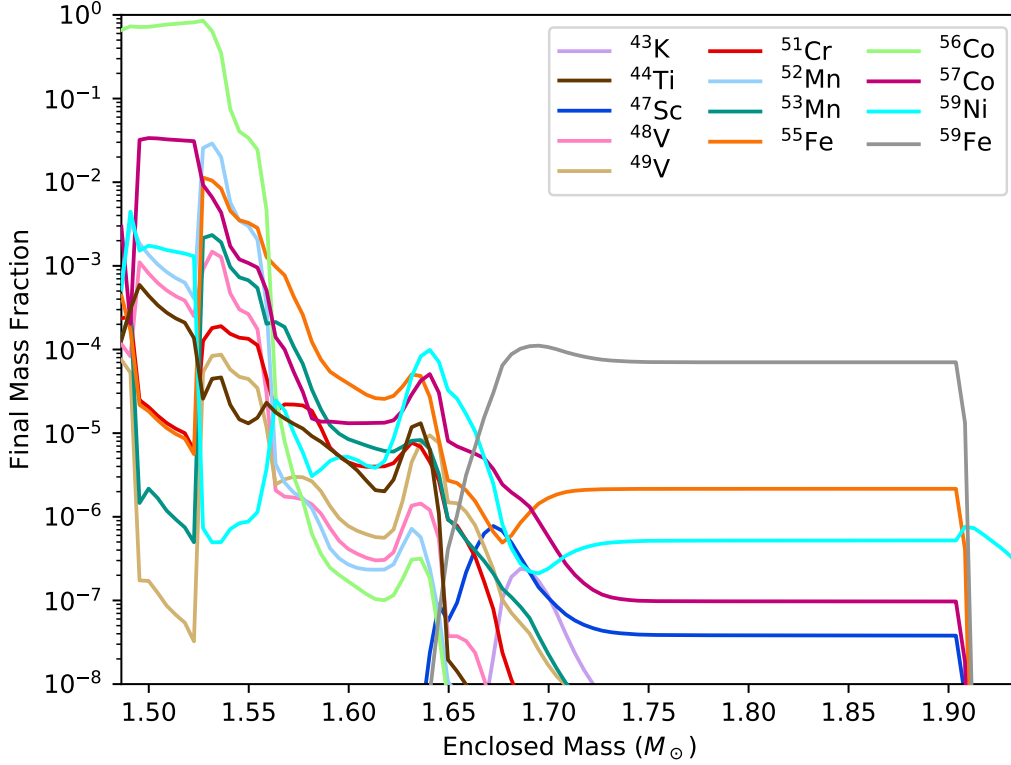
Figure 3. Final mass fractions of isotopes of interest by enclosed mass shell for evolutions using standard REACLIB rates. Mass fractions include the short-lived parent isotopes in the mass chain (e.g. ^{56}Co includes both ^{56}Co and ^{56}Ni). Only the simulated region of enclosed mass is shown.
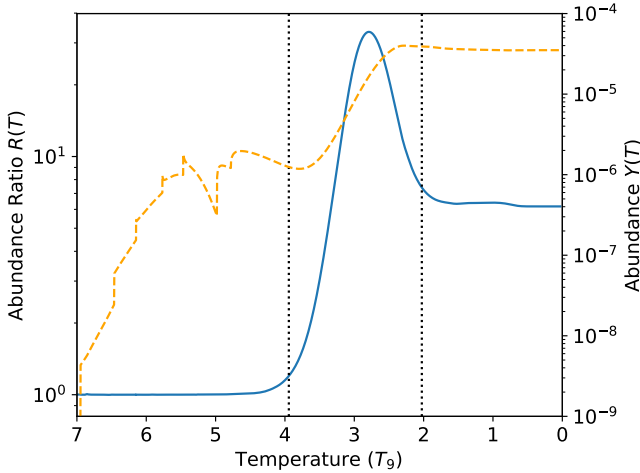

Figure 4. $A = 44$ abundance (orange dashed line) and ratio of $A = 44$ abundance to the baseline abundance when varying ^{44}Ti$(\alpha,\text{p})^{47}$V by x0.01 as functions of temperature (blue line). Dotted black vertical lines indicate the determined temperature range where the reaction affects ^{44}Ti production.

ations varies widely. The lighter isotopes in the $A = 43 - 49$ mass range are affected by a larger number of reaction rates.

The most sensitive isotope is the lightest and most neutron-rich isotope studied here, ^{43}K. When varied by a factor of a 100, 20 reaction rates have $F_i \geq 2$, and 19 additional reaction rates have $F_i \geq 1.3$. For the other interesting isotopes in this mass range, 47 reaction rates have $F_i \geq 1.3$ for at least one isotope i. On the other hand, for each of the isotopes in the $A = 52 - 57$ mass range, there are no reaction rates with $F_i \geq 2$, and only 8 with $F_i \geq 1.3$. The $A = 52 - 57$ isotopes are closer to the peak of the NSE abundance distribution at $A = 56$. Their synthesis is therefore more dominated by NSE, making them less susceptible to reaction rate variations.

The most impactful reactions fall generally into two categories: reactions involving the isotope of interest or its parent nuclei, and rates which affect explosive nucleosynthesis more broadly. Reactions in the latter category are listed in Table 2. This group includes the strongest sensitivity identified in this study, the impact of the ^{24}Mg$(\text{n},\gamma)^{25}$Mg reaction on ^{43}K production. This reaction affects the production of all neutron-rich isotopes of interest. For the proton-rich isotopes, the reactions with the broadest impact are $\alpha(2\alpha,\gamma)^{12}$C, ^{13}N$(\alpha,\text{p})^{16}$O, ^{16}O$(^{12}C,p)^{27}$Al, and ^{12}C$(\alpha,\gamma)^{16}$O, each of which significantly affects the production of 7 or more of the 13 isotopes of interest. The reactions are bottle-

Table 2. Reaction rate variations that affect three or more isotopes of interest

Reaction	Number of Isotopes Affected
^{12}C(α,γ)^{16}O	8
$\alpha(2\alpha,\gamma)^{12}$C	8
^{16}O(^{12}C,p)^{27}Al	8
^{13}N(α,p)^{16}O	7
^{27}Al(α,n)^{30}P	6
^{20}Ne(α,γ)^{24}Mg	6
^{44}Ti(α,p)^{47}V	5
^{42}Ca(α,γ)^{46}Ti	5
^{16}O(^{12}C,α)^{24}Mg	5
^{48}Cr(α,p)^{51}Mn	4
^{23}Na(α,p)^{26}Mg	4
^{53}Fe(n,p)^{53}Mn	3
^{52}Fe(α,p)^{55}Co	3
^{33}S(n,α)^{30}Si	3
^{30}Si(p,γ)^{31}P	3
^{28}Si(n,γ)^{29}Si	3
^{28}Al(p,α)^{25}Mg	3
^{27}Si(n,^{12}C)^{16}O	3
^{27}Al(α,p)^{30}Si	3
^{26}Mg(α,n)^{29}Si	3
^{25}Mg(p,γ)^{26}Al	3
^{25}Mg(n,γ)^{26}Mg	3
^{25}Mg(α,n)^{28}Si	3
^{24}Mg(n,γ)^{25}Mg	3
^{20}Ne(n,γ)^{21}Ne	3
^{16}O(α,γ)^{20}Ne	3

necks in the build-up of heavy elements during NSE freeze-out.

The other category of impactful reactions includes reactions which directly involve the isotope of interest or its parent nuclei. These include reactions like ^{42}K(n,γ)^{43}K, ^{47}Sc(n,γ)^{48}Sc, ^{49}Mn(p,γ)^{50}Fe, ^{51}Mn(p,γ)^{52}Fe, ^{52}Fe(α,p)^{55}Co, ^{53}Fe(n,p)^{53}Mn, ^{55}Co(p,γ)^{56}Ni, ^{57}Ni(n,p)^{57}Co, and ^{59}Cu(p,γ)^{60}Zn, which all are among the most impactful reactions for their respective isotopes, and for these isotopes only. By nature these reactions involve radioactive isotopes. ^{44}Ti(α,p)^{47}V and ^{48}Cr(α,p)^{51}Mn are somewhat an exception falling into both categories. While they have the strongest impact on ^{44}Ti and ^{51}Cr production, respectively, they also impact a number of other isotopes of interest (see Table 2).

Table 1 also lists for each reaction rate variation the temperature range where the change in reaction rate produces the change in final abundance. This is the estimated temperature range over which the reaction rate needs to be known in order to predict nucleosynthesis reliably. These temperatures are mostly between 0.7 GK and 5.5 GK for all reactions. The $\alpha(2\alpha,\gamma)^{12}$C reaction is an exception, often leading to changes at temperatures up to and above 6 GK. The typical temperature ranges depend strongly on the isotope of interest. For ^{43}K, ^{47}Sc, ^{59}Fe, and ^{59}Ni the temperature range of interest is quite narrow (1.4 - 2.7 GK). The only outlier in that group is the ^{57}Cu(p,γ)^{58}Zn reaction affecting ^{59}Ni at relatively low temperatures of 0.8 - 1.1 GK. For ^{44}Ti, ^{48}V, ^{49}V, and ^{51}Cr the temperature range of interest is much broader (mostly 0.7 - 5 GK). For ^{52}Mn, ^{53}Mn, ^{55}Fe, and ^{57}Co the temperature range is narrower but higher (2.0 - 5.5 GK) with two exceptions - the ^{52}Fe(p,γ)^{53}Co reaction affects ^{53}Mn at 0.73 - 1 GK, and the ^{56}Ni(p,γ)^{57}Co reaction affects ^{57}Co at very low temperatures of 0.47 - 0.65 GK.

5. DISCUSSION

5.1. *Nucleosynthesis*

Figure 5 displays a comparison of the ejected masses of the mass chains of interest produced in the current model with two examples from previous work, Sukhbold et al. (2016) and Curtis et al. (2019). Figure 6 displays the ratios to solar abundances up to $A = 80$. All three use a 12 $M_\odot$ progenitor, we take the progenitors evolved in Sukhbold et al. (2016), which are based on Woosley & Heger (2015), while Curtis et al. (2019) uses Woosley & Heger (2007) progenitors. In terms of nuclear physics, Curtis et al. (2019) also uses REACLIB reaction rates, while Sukhbold et al. (2016) uses older rates as in Woosley & Heger (2007). The results from different models agree mostly within 40%, except for $A = 48$ where there is a 80% difference between our result and the result of Sukhbold et al. (2016). While differences with respect to Sukhbold et al. (2016) could be in part due to use of different reaction rates, clearly there are also astrophysical uncertainties in the prediction of nucleosynthesis from explosive Si burning.

The ^{44}Ti yield in this work of 1.4×10^{-5} $M_\odot$ is about an order of magnitude lower than that inferred from observations of SN1987a or Cas A, in line with previous 1D supernova model calculations (see Figure 5 and, for example, the summary in Chieffi & Limongi (2017)).

5.2. *Previous Sensitivity Studies*

5.2.1. *^{44}Ti*

Given the importance of ^{44}Ti for γ-ray observations, a number of previous studies have identified critical nuclear reactions affecting its production, in particular the studies of The et al. (1998) and Magkotsios et al. (2010). All studies, including this work, agree that ^{44}Ti(α,p)^{47}V, ^{40}Ca(α,γ)^{44}Ti and $\alpha(2\alpha,\gamma)^{12}$C are the most important reactions governing the production of ^{44}Ti. There is also agreement that the
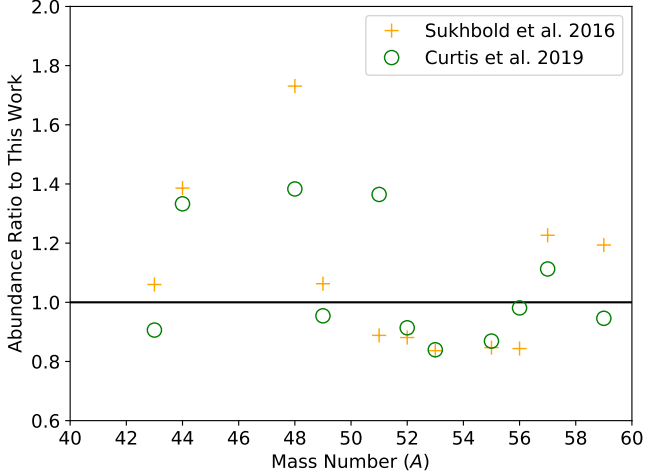
Figure 5. Ratio of mass fraction of ejected isotopes in previous studies (Sukhbold et al. 2016; Curtis et al. 2019) to this work, summed by mass number.
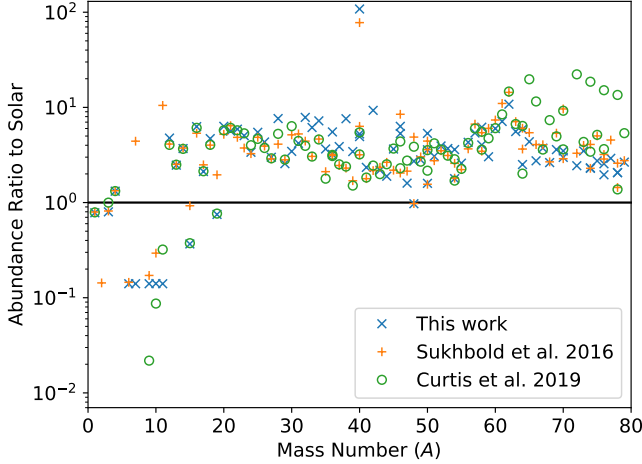

Figure 6. Ratio of abundances of ejected isotopes to solar abundances summed by mass number.

^{45}V(p,γ)^{46}Cr reactions plays a role, even though our model is much less sensitive to this reaction than both The et al. (1998) and Magkotsios et al. (2010), where this reaction ranks near the top. On the other hand, we do find a significant sensitivity to ^{44}Ti(p,γ)^{45}V, as does Magkotsios et al. (2010), indicating that in our model (p,γ)-(γ,p) equilibrium between ^{44}Ti and ^{45}V is not well established during ^{44}Ti synthesis.

For the remaining reactions identified in this work there are significant differences with The et al. (1998). Most of our sensitive reactions do not appear in their study, and we do not find the strong sensitivity to the ^{44}Ti(α,γ)^{48}Cr, ^{57}Ni(p,γ)^{58}Cu, and ^{57}Co(p,n)^{57}Ni reactions that they found. The et al. (1998) used a much narrower range of conditions and evolved a pure initial ^{28}Si composition from NSE conditions at T = 5.5 GK and ρ = 10^7 g cm^{-3} through adiabatic expansion. In contrast,

our model utilizes several initial compositions and thermodynamic trajectories, only the first ≈ 0.03 $M_\odot$ of which achieve the NSE conditions of The et al. (1998). Our model therefore includes both complete and incomplete explosive burning. Even so, we do find a weak sensitivity on ^{44}Ti(α,γ)^{48}Cr of $F_i \sim 1.08$ (when varied by a factor of 100), just below our threshold.

Overall our results agree more closely with Magkotsios et al. (2010), who scan a broad selection of peak temperatures and densities, indicating that more realistic models are needed to identify reaction rate sensitivities for ^{44}Ti. There are only 4 out of 15 reactions in our list that do not appear in Magkotsios et al. (2010): ^{39}K(p,α)^{36}Ar, ^{27}Al(α,n) ^{30}P, ^{42}Ca(p,α)^{39}K, and ^{32}S(n,α)^{30}Si. However, ^{39}K(p,α)^{36}Ar does appear prominently in The et al. (1998). There are also three reactions that are ranked as "Primary" in Magkotsios et al. (2010) that we do not find to have a strong sensitivity: ^{17}F(α,p)^{20}Ne, ^{21}Na(α,p)^{24}Mg, and again ^{57}Ni(p,γ)^{58}Cu. ^{57}Ni(p,γ)^{58}Cu has $F_i \sim 1.03$, just below our threshold. They find the other two reactions to be significant only in regions of higher peak densities ($\rho \sim 10^9$ g cm^{-3}) than our conditions.

5.2.2. ^{55}Fe, ^{57}Co, ^{59}Ni

Reactions relevant for ^{55}Fe, ^{57}Co, and ^{59}Ni production were identified in Jordan et al. (2003), who use a similar exponential expansion model as The et al. (1998). For ^{55}Fe, we find only one of the four rates identified in Jordan et al. (2003), ^{55}Co(p,γ)^{56}Ni, to be significant. Of the three others, $\alpha(2\alpha,\gamma)^{12}$C is found to cause a $F_i \sim 1.09$ effect at a factor of x100 change, and both ^{59}Cu(p,α)^{56}Ni, and ^{59}Cu(p,γ)^{60}Zn have only a minimal effect. As before, the simplified model and the more limited range of conditions explored in Jordan et al. (2003) are likely the reason for the discrepancy. Much of the ^{55}Fe production in our model occurs in the trajectories which do not undergo complete burning and do not reach the temperatures or densities specified in Jordan et al. (2003). Because of this, we generate a higher mass fraction ($\sim$ x10) of ^{55}Fe than Jordan et al. (2003), and obtain a more complete picture of ^{55}Fe production. For ^{57}Co and ^{59}Ni our results agree with Jordan et al. (2003) on the most important reactions, ^{57}Ni(n,p)^{57}Co in the case of ^{57}Co and ^{59}Cu (p,γ)^{60}Zn, ^{59}Cu(p,α)^{56}Ni and $\alpha(2\alpha,\gamma)^{12}$C in the case of ^{59}Ni. For all three isotopes we explore not only x10 variations as in Jordan et al. (2003), but also x100 variations. Consequently we identify a number of additional relevant reactions.

5.3. Rate Uncertainties

The main goal of this paper is to identify the nuclear reaction rates that determine long-lived radioisotope production in CCSNe. However, to provide guidance for nuclear physics on which of these reaction rates need improved accuracy,

their current uncertainties must be considered. Such uncertainties are often difficult to estimate reliably, especially in the case of theoretical predictions. Nevertheless, to provide some approximate guidance, we used the uncertainty factors listed in the current STARLIB database (Sallaska et al. 2013) for the relevant temperature ranges that we identified in this work. While past studies (Fields et al. 2018) used Monte Carlo methods to sample STARLIB rates within the prescribed uncertainties, here we take a more simplified approach. We interpolated our sensitivities in Table 1 and determined the expected final abundance changes for rate variations within the STARLIB 1σ uncertainty (the impact factor). We considered both rate increases and rate decreases and used the larger sensitivity. Table 3 provides a list of reactions ordered by their impact factor, F_i, for $F_i \geq 1.1$. 16 reactions have $F_i \geq 1.5$. Reactions with large impact factors indicate the most important reaction rate uncertainties to be addressed for improved nucleosynthesis predictions.

We emphasize that the impact factors provide only some approximate guidance. In addition to astrophysical uncertainties and possible correlations between rate uncertainties, there are large uncertainties in the estimates of the reaction rate uncertainties. For example, the $\alpha(2\alpha,\gamma)^{12}$C reaction does not appear in this list despite its importance, as its uncertainty in STARLIB is less than 35%. However, this rate needs to be known up to a temperature of around 5.8 GK. At such high temperatures, the role of resonances above the Hoyle state in ^{12}C remains unclear and uncertainties are likely underestimated considerably (Zimmerman et al. 2013). In addition, it has been pointed out, that proton induced scattering at sufficiently high densities and temperatures can lead to orders of magnitude increases in the $\alpha(2\alpha,\gamma)^{12}$C reaction rate (Beard et al. 2017). The impact of these effects, and their uncertainties, needs to be investigated. The sensitivities provided in Table 1 can then be used to determine whether an improved reaction rate is needed for explosive Si burning nucleosynthesis.

Table 3. Reaction rates with the largest impact based on their current estimated uncertainties.

Reaction	Impact	Isotope Affected
^{42}K(n,γ)^{43}K	4.18	^{43}K
^{44}Ti(α,p)^{47}V	2.61, 1.31, 1.12[a]	^{44}Ti, ^{48}V, ^{49}V
^{43}K(p,n)^{43}Ca	2.51	^{43}K
^{59}Cu(p,γ)^{60}Zn	2.16	^{59}Ni
^{42}K(p,n)^{42}Ca	2.13	^{43}K
^{23}Na(α,p)^{26}Mg	2.12, 1.14, 1.13, 1.12[a]	^{43}K, ^{47}Sc ^{49}V, ^{55}Fe
^{27}Al(α,p)^{30}Si	1.91, 1.58[a]	^{43}K, ^{47}Sc
^{28}Al(p,α)^{25}Mg	1.89, 1.37[a]	^{43}K, ^{47}Sc

Table 3 *continued*

Table 3 *(continued)*

Reaction	Impact	Isotope Affected
^{47}Sc(n,γ)^{48}Sc	1.88	^{47}Sc
^{47}Ti(n,p)^{47}Sc	1.85	^{47}Sc
^{48}Cr(α,p)^{51}Mn	1.84, 1.16[a]	^{48}V, ^{51}Cr
^{51}Mn(p,γ)^{52}Fe	1.76	^{51}Cr
^{41}K(p,α)^{38}Ar	1.72	^{43}K
^{43}K(n,γ)^{44}K	1.65	^{43}K
^{46}Sc(n,γ)^{47}Sc	1.55	^{47}Sc
^{46}Sc(p,n)^{46}Ti	1.45	^{47}Sc
^{53}Fe(n,p)^{53}Mn	1.41	^{53}Mn
^{49}Mn(p,γ)^{50}Fe	1.34	^{49}V
^{55}Co(p,γ)^{56}Ni	1.32	^{55}Fe
^{45}Ca(n,γ)^{46}Ca	1.31	^{47}Sc
^{32}S(n,α)^{29}Si	1.31, 1.29[a]	^{43}K, ^{47}Sc
^{40}Ar(p,γ)^{41}K	1.30	^{43}K
^{44}Ca(p,γ)^{45}Sc	1.29	^{47}Sc
^{40}K(n,γ)^{41}K	1.29	^{43}K
^{45}Sc(p,γ)^{46}Ti	1.27	^{47}Sc
^{59}Cu(p,α)^{56}Ni	1.25	^{59}Ni
^{49}Cr(n,p)^{49}V	1.25	^{49}V
^{57}Ni(n,p)^{57}Co	1.24, 1.21[a]	^{57}Co, ^{59}Ni
^{41}Ca(n,α)^{38}Ar	1.23	^{43}K
^{41}K(p,n)^{41}Ca	1.21	^{43}K
^{59}Fe(n,γ)^{60}Fe	1.19	^{59}Fe
^{49}V(p,γ)^{50}Cr	1.19	^{49}V
^{25}Mg(α,n)^{28}Si	1.19, 1.11[a]	^{47}Sc, ^{43}K
^{43}Sc(p,γ)^{44}Ti	1.18	^{44}Ti
^{57}Cu(p,γ)^{58}Zn	1.17	^{59}Ni
^{46}Ca(p,γ)^{47}Sc	1.16	^{47}Sc
^{52}Fe(α,p)^{55}Co	1.15	^{52}Mn
^{48}Cr(p,γ)^{49}Mn	1.15	^{49}V
^{43}Sc(p,α)^{40}Ca	1.15	^{44}Ti
^{41}Ca(n,γ)^{42}Ca	1.15	^{47}Sc
^{39}Ar(n,γ)^{40}Ar	1.15	^{43}K
^{28}Al(p,n)^{28}Si	1.15	^{43}K
^{13}N(α,p)^{16}O	1.15, 1.15, 1.14, 1.14, 1.11[a]	^{52}Mn, ^{55}Fe, ^{49}V, ^{53}Mn, ^{48}V
^{49}Cr(p,γ)^{50}Mn	1.14	^{49}V
^{40}Ca(α,γ)^{44}Ti	1.14	^{44}Ti
^{41}K(p,γ)^{42}Ca	1.13	^{43}K
^{47}Ca(p,n)^{47}Sc	1.11	^{47}Sc
^{45}V(p,γ)^{46}Cr	1.10	^{44}Ti

[a] For reactions that impact multiple isotopes of interest, the impact numbers correspond to the isotopes listed, respectively.

6. CONCLUSION

We determined the sensitivity of the production of long-lived radioactive isotopes in a model for explosive Si burning in a CCSN. We vary individual reaction rates to determine the local derivative of the final abundance of a given isotope

with respect to a given reaction rate. This approach has been used in previous work (e.g., Iliadis et al. (2002)) and enables the identification of critical reaction rates without making assumptions about their uncertainties. Compared to previous studies, we investigate the synthesis of a much broader range of 13 radioisotopes from ^{43}K to ^{59}Ni using a new model for 1D CCSN explosions that incorporates the crucial effects of convection and turbulence and does not resort to altering the microphysics to achieve explosions (Couch et al. 2020). We also developed a new method to identify the relevant temperature range for each reaction, and find that these temperature ranges depend sensitively on the reaction and final isotope of interest. Our results can be used to determine the importance of a given reaction rate uncertainty (in the relevant temperature range provided by our work) for CCSN explosive nucleosynthesis predictions, and provide guidance on which reactions require further study, both experimental and theoretical. This is of particular importance in light of new emerging capabilities in nuclear experiment and nuclear theory. To provide some initial guidance in this direction, we use the reaction rate uncertainties provided by the STARLIB database to produce a ranked list of the most important reaction rate uncertainties. We emphasize however that for a final decision on the importance of a reaction rate a thorough analysis of the possible uncertainties is required, as well as considerations of the individual accuracy needs for the various long-lived radioactive isotopes.

The future reduction of nuclear physics uncertainties in explosive Si burning nucleosynthesis models enabled by our work will be important to prepare the field for advances in X- and γ-ray observations (Timmes et al. 2019), in stardust analysis (Stephan et al. 2016), and for the potential observation of a galactic supernova. Reduced and well characterized nuclear physics uncertainties will enable quantitative comparisons of astrophysical models with observations. While our results for ^{44}Ti are in overall reasonable agreement with the one previous study (Magkotsios et al. 2010) that explored a similar realistic range of conditions, there are some differences, especially for the weaker sensitivities. This may indicate that a broader range of sensitivity studies for different astrophysical models may be needed to identify the individual nuclear physics needs of each model.

Table 1. Final Abundance Changes Resulting from Reaction-Rate Variations

Isotope	$X_{i,\mathrm{rec}}$	Reaction	R_f For Reaction Rate Multiplied By:						T_9 Range	
			100	10	2	0.5	0.1	0.01	$T_{9,\mathrm{low}}$	$T_{9,\mathrm{high}}$
^{43}K	1.4e-08	^{24}Mg(n,γ)^{25}Mg	0.139	0.196	0.571	1.61	3.12	4.01	1.39	2.38
		^{42}K(n,γ)^{43}K	3.97	2.93	1.54	0.622	0.239	0.139	1.39	2.38
		^{25}Mg(α,n)^{28}Si	6.94	4.47	1.62	0.697	0.484	0.443	2.15	2.4
		^{25}Mg(n,γ)^{26}Mg	0.166	0.333	0.764	1.2	1.47	1.55	1.41	2.38
		^{43}K(p,n)^{43}Ca	0.172	0.398	0.771	1.26	1.95	2.78	1.42	2.6
		^{20}Ne(n,γ)^{21}Ne	0.2	0.51	0.892	1.07	1.12	1.14	1.44	2.45
		^{42}K(p,n)^{42}Ca	0.203	0.47	0.828	1.16	1.39	1.49	1.44	2.45
		^{25}Mg(p,γ)^{26}Al	0.222	0.452	0.872	1.08	1.17	1.19	1.46	2.4
		^{41}K(n,γ)^{42}K	3.62	2.79	1.49	0.666	0.333	0.247	1.47	2.38
		^{28}Al(p,α)^{25}Mg	4.04	1.89	1.12	0.941	0.894	0.884	2.14	2.4
		^{23}Na(α,p)^{26}Mg	0.259	0.471	0.821	1.16	1.4	1.48	1.47	2.38
		^{27}Al(α,p)^{30}Si	0.294	0.523	0.857	1.12	1.27	1.32	2.06	2.4
		^{20}Ne(α,γ)^{24}Mg	0.3	0.525	0.855	1.12	1.26	1.31	2.1	2.6

Table 1 *continued*

HERMANSEN ET AL.

Table 1 *(continued)*

| Isotope | $X_{i,\text{rec}}$ | Reaction | \multicolumn{6}{c}{R_f For Reaction Rate Multiplied By:} | \multicolumn{2}{c}{T_9 Range} |
			100	10	2	0.5	0.1	0.01	$T_{9,\text{low}}$	$T_{9,\text{high}}$
		^{41}K(p,α)^{38}Ar	0.313	0.581	0.884	1.09	1.19	1.22	2.09	2.38
		^{43}K(n,γ)^{44}K	0.315	0.605	0.911	1.06	1.11	1.12	2.11	2.38
		^{28}Si(n,γ)^{29}Si	0.322	0.742	0.954	1.03	1.05	1.06	2.17	2.38
		^{26}Mg(α,n)^{29}Si	2.94	2.29	1.35	0.76	0.539	0.489	2.15	2.38
		^{27}Al(p,γ)^{28}Si	2.53	1.41	1.05	0.972	0.949	0.943	2.14	2.48
		^{27}Al(n,γ)^{28}Al	2.02	1.3	1.04	0.981	0.967	0.964	2.1	2.48
		^{29}Si(n,γ)^{30}Si	0.499	0.797	0.962	1.02	1.04	1.05	2.17	2.38
		^{24}Mg(α,γ)^{28}Si	1.93	1.14	1.02	0.991	0.985	0.984	2.09	2.48
		^{23}Na(p,α)^{20}Ne	1.09	1.08	1.04	0.935	0.721	0.53	2.15	2.38
		^{30}Si(p,γ)^{31}P	1.82	1.42	1.07	0.962	0.93	0.923	2.11	2.56
		^{41}K(p,γ)^{42}Ca	0.55	0.886	0.984	1.01	1.01	1.02	2.12	2.38
		^{21}Ne(α,n)^{24}Mg	1.07	1.06	1.03	0.95	0.764	0.582	2.24	2.38
		^{27}Al(p,α)^{24}Mg	0.762	0.796	0.904	1.13	1.44	1.67	2.14	2.48
		^{29}Si(p,γ)^{30}P	0.621	0.832	0.968	1.02	1.04	1.04	2.14	2.38
		^{40}Ar(p,γ)^{41}K	1.6	1.3	1.07	0.951	0.899	0.885	2.13	2.38
		^{32}S(n,α)^{29}Si	1.59	1.31	1.06	0.969	0.944	0.938	2.17	2.4
		^{40}K(n,γ)^{41}K	1.57	1.29	1.06	0.968	0.94	0.933	2.15	2.38
		^{40}Ca(n,γ)^{41}Ca	1.54	1.31	1.07	0.957	0.918	0.909	2.15	2.38
		^{21}Ne(p,γ)^{22}Na	0.71	0.925	0.992	1.0	1.01	1.01	2.22	2.38
		^{41}K(p,n)^{41}Ca	1.37	1.21	1.04	0.974	0.95	0.945	2.27	2.38
		^{28}Al(p,n)^{28}Si	1.04	1.03	1.02	0.973	0.869	0.747	2.14	2.38
		^{41}Ca(n,α)^{38}Ar	0.893	0.905	0.953	1.07	1.23	1.33	2.15	2.38
		^{39}Ar(n,γ)^{40}Ar	1.32	1.15	1.03	0.986	0.973	0.97	2.15	2.38
		^{39}K(n,γ)^{40}K	1.31	1.19	1.05	0.971	0.944	0.937	2.17	2.38
		^{26}Mg(p,γ)^{27}Al	1.14	1.29	1.11	0.909	0.797	0.763	2.06	2.38
		^{37}Cl(α,γ)^{41}K	1.3	1.03	1.0	0.998	0.997	0.997	2.17	2.38
		^{16}O(α,γ)^{20}Ne	1.07	1.05	1.02	0.96	0.905	0.803	2.02	2.6
		^{27}Al(α,n)^{30}P	0.803	0.957	0.994	1.0	1.01	1.01	2.11	2.38
		^{16}O(^{12}C,p)^{27}Al	0.806	0.975	0.997	1.0	1.0	1.0	2.14	2.38
		^{32}S(n,γ)^{33}S	0.819	0.899	0.977	1.02	1.03	1.04	2.21	2.38
		^{12}C(^{12}C,α)^{20}Ne	1.21	1.04	1.0	0.997	0.995	0.995	1.98	2.38
		^{29}Si(α,γ)^{33}S	0.841	0.976	0.997	1.0	1.0	1.0	2.15	2.38
		^{38}Ar(p,γ)^{39}K	1.18	1.07	1.01	0.992	0.985	0.983	2.15	2.38
		^{42}K(p,α)^{39}Ar	0.848	0.982	0.998	1.0	1.0	1.0	2.12	2.38
		^{30}Si(n,γ)^{31}Si	1.15	1.03	1.0	0.998	0.997	0.997	2.1	2.4
		^{39}Ar(p,γ)^{40}K	1.15	1.04	1.01	0.997	0.995	0.994	2.15	2.38
		^{22}Ne(α,n)^{25}Mg	1.02	1.02	1.01	0.981	0.916	0.874	2.17	2.38
		^{28}Al(n,γ)^{29}Al	0.878	0.978	0.997	1.0	1.0	1.0	2.21	2.38
		^{23}Na(α,γ)^{27}Al	0.885	0.986	0.998	1.0	1.0	1.0	2.17	2.38
		^{21}Ne(n,γ)^{22}Ne	0.893	0.987	0.998	1.0	1.0	1.0	2.24	2.38
		^{26}Al(n,p)^{26}Mg	0.922	0.933	0.97	1.03	1.1	1.12	2.15	2.38
		^{43}K(p,α)^{40}Ar	0.901	0.989	0.999	1.0	1.0	1.0	2.1	2.38
		^{41}Ca(n,γ)^{42}Ca	0.904	0.962	0.994	1.0	1.01	1.01	2.15	2.38
		^{40}K(n,α)^{37}Cl	0.907	0.924	0.971	1.03	1.06	1.07	2.15	2.38
		^{23}Na(n,γ)^{24}Na	0.908	0.97	0.996	1.0	1.0	1.0	2.05	2.38
		^{38}Ar(n,γ)^{39}Ar	1.1	1.06	1.01	0.991	0.983	0.981	2.12	2.38

Table 1 *continued*

Table 1 *(continued)*

| Isotope | $X_{i,\text{rec}}$ | Reaction | R_f For Reaction Rate Multiplied By: | | | | | | T_9 Range | |
			100	10	2	0.5	0.1	0.01	$T_{9,\text{low}}$	$T_{9,\text{high}}$
^{44}Ti	3.01e-05	^{44}Ti$(\alpha,$p$)^{47}$V	0.209	0.385	0.74	1.35	2.61	5.74	0.88	3.94
		$\alpha(2\alpha,\gamma)^{12}$C	1.3	1.0	1.01	0.929	0.528	0.175	1.83	6.15
		^{40}Ca$(\alpha,\gamma)^{44}$Ti	1.96	1.62	1.19	0.83	0.543	0.374	0.97	3.21
		^{12}C$(\alpha,\gamma)^{16}$O	2.15	1.2	1.02	0.988	0.977	0.975	2.1	4.98
		^{43}Sc$(p,\gamma)^{44}$Ti	1.35	1.18	1.04	0.977	0.958	0.951	1.66	3.09
		^{13}N$(\alpha,$p$)^{16}$O	1.29	1.05	1.01	0.994	0.992	1.01	2.08	4.98
		^{43}Sc$(p,\alpha)^{40}$Ca	0.949	0.958	0.979	1.03	1.15	1.28	1.79	2.39
		^{27}Al$(\alpha,$n$)^{30}$P	0.787	0.952	0.994	1.0	1.01	1.01	1.22	3.14
		^{39}K$(p,\alpha)^{36}$Ar	1.02	1.01	1.01	0.991	0.941	0.849	1.35	2.64
		^{42}Ca$(p,\alpha)^{39}$K	1.17	1.08	1.02	0.983	0.966	0.961	1.93	2.74
		^{44}Ti$(p,\gamma)^{45}$V	0.864	0.923	0.978	1.02	1.05	1.14	0.69	1.77
		^{41}Sc$(p,\gamma)^{42}$Ti	1.15	1.03	1.0	1.0	1.02	1.08	0.58	1.56
		^{33}S$(n,\alpha)^{30}$Si	0.89	0.967	0.995	1.0	1.01	1.01	1.69	3.11
		^{11}B$(\alpha,$n$)^{14}$N	0.9	0.969	0.997	1.0	1.01	1.0	2.13	3.19
		^{45}V$(p,\gamma)^{46}$Cr	0.902	0.906	0.956	1.04	1.09	1.11	0.93	2.39
^{47}Sc	6.12e-08	^{47}Sc$(n,\gamma)^{48}$Sc	0.361	0.531	0.849	1.12	1.25	1.29	1.37	2.6
		^{25}Mg$(\alpha,$n$)^{28}$Si	2.61	1.92	1.24	0.83	0.66	0.619	1.42	2.6
		^{47}Ti$(n,$p$)^{47}$Sc	0.408	0.546	0.813	1.24	1.85	2.23	1.38	2.71
		^{24}Mg$(n,\gamma)^{25}$Mg	0.462	0.537	0.811	1.21	1.65	1.91	1.39	2.65
		^{30}Si$(p,\gamma)^{31}$P	2.08	1.77	1.21	0.866	0.745	0.716	2.13	2.65
		^{28}Si$(n,\gamma)^{29}$Si	0.49	0.744	0.944	1.04	1.07	1.08	1.39	2.6
		^{27}Al$(\alpha,$p$)^{30}$Si	0.495	0.631	0.867	1.13	1.35	1.44	1.39	2.65
		^{27}Al$(p,\gamma)^{28}$Si	2.01	1.43	1.07	0.964	0.934	0.926	2.16	2.65
		^{20}Ne$(\alpha,\gamma)^{24}$Mg	0.503	0.693	0.898	1.1	1.31	1.41	1.41	2.65
		^{25}Mg$(p,\gamma)^{26}$Al	0.51	0.619	0.874	1.1	1.2	1.23	1.41	2.6
		^{46}Sc$(n,\gamma)^{47}$Sc	1.95	1.55	1.15	0.892	0.778	0.748	2.27	2.65
		^{25}Mg$(n,\gamma)^{26}$Mg	0.522	0.671	0.897	1.09	1.2	1.23	1.41	2.6
		^{28}Al$(p,\alpha)^{25}$Mg	1.87	1.37	1.06	0.964	0.934	0.927	2.21	2.6
		^{24}Mg$(\alpha,\gamma)^{28}$Si	1.8	1.27	1.04	0.981	0.966	0.963	2.18	2.65
		^{46}Sc$(p,$n$)^{46}$Ti	0.556	0.692	0.895	1.1	1.29	1.38	1.41	2.65
		^{27}Al$(p,\alpha)^{24}$Mg	0.929	0.93	0.962	1.07	1.36	1.77	2.17	2.65
		^{16}O$(\alpha,\gamma)^{20}$Ne	1.1	1.07	1.02	0.989	0.912	0.568	1.41	2.65
		^{20}Ne$(n,\gamma)^{21}$Ne	0.576	0.766	0.95	1.03	1.06	1.07	1.41	2.6
		^{46}Ca$(n,\gamma)^{47}$Ca	1.73	1.34	1.07	0.962	0.928	0.92	2.1	2.51
		^{45}Sc$(n,\gamma)^{46}$Sc	1.46	1.37	1.14	0.859	0.654	0.585	1.41	2.65
		^{27}Al$(n,\gamma)^{28}$Al	1.68	1.17	1.02	0.99	0.982	0.98	2.18	2.6
		^{26}Mg$(\alpha,$n$)^{29}$Si	1.22	1.19	1.09	0.891	0.688	0.613	1.42	2.6
		^{45}Sc$(p,\gamma)^{46}$Ti	0.623	0.787	0.945	1.04	1.09	1.11	1.63	2.6
		^{29}Si$(n,\gamma)^{30}$Si	0.632	0.83	0.966	1.02	1.04	1.04	2.06	2.6
		^{44}Ca$(p,\gamma)^{45}$Sc	1.55	1.29	1.08	0.939	0.861	0.835	2.21	2.6
		^{45}Ca$(n,\gamma)^{46}$Ca	1.49	1.31	1.08	0.948	0.898	0.886	2.38	2.6
		^{29}Si$(p,\gamma)^{30}$P	0.672	0.777	0.938	1.04	1.09	1.1	2.12	2.6
		^{42}Ca$(p,\alpha)^{39}$K	1.4	1.08	1.01	0.995	0.991	0.99	2.2	2.65
		^{32}S$(n,\alpha)^{29}$Si	1.37	1.29	1.11	0.916	0.836	0.82	2.15	2.6
		^{44}Ca$(n,\gamma)^{45}$Ca	1.36	1.27	1.08	0.943	0.884	0.869	2.24	2.6
		^{26}Mg$(p,\gamma)^{27}$Al	0.734	0.871	0.983	0.999	0.974	0.96	2.45	2.6

Table 1 *continued*

Table 1 *(continued)*

Isotope	$X_{i,\text{rec}}$	Reaction	R_f For Reaction Rate Multiplied By:						T_9 Range	
			100	10	2	0.5	0.1	0.01	$T_{9,\text{low}}$	$T_{9,\text{high}}$
		^{41}Ca(n,γ)^{42}Ca	1.36	1.15	1.02	0.987	0.976	0.973	2.21	2.6
		^{23}Na(α,p)^{26}Mg	0.736	0.875	0.979	1.01	1.0	0.997	2.14	2.66
		^{46}Sc(p,γ)^{47}Ti	0.755	0.948	0.993	1.0	1.01	1.01	2.16	2.6
		^{29}Si(α,γ)^{33}S	0.758	0.941	0.992	1.0	1.01	1.01	2.15	2.6
		^{32}S(n,γ)^{33}S	0.76	0.835	0.945	1.06	1.17	1.22	2.17	2.65
		^{46}Ca(p,γ)^{47}Sc	1.28	1.13	1.04	0.955	0.862	0.82	2.09	2.6
		^{30}Si(n,γ)^{31}Si	1.21	1.04	1.0	0.998	0.996	0.996	2.18	2.6
		^{38}Ar(α,γ)^{42}Ca	1.2	1.02	1.0	0.999	0.998	0.998	2.19	2.65
		^{47}Ca(p,n)^{47}Sc	0.95	0.96	0.982	1.03	1.11	1.19	2.19	2.6
		^{21}Ne(α,n)^{24}Mg	1.02	1.01	1.01	0.991	0.946	0.85	2.4	2.56
		^{47}Sc(p,γ)^{48}Ti	0.859	0.983	0.998	1.0	1.0	1.0	2.17	2.6
		^{28}Si(α,γ)^{32}S	0.861	0.962	0.993	1.0	1.01	1.01	2.21	2.6
		^{31}P(α,p)^{34}S	0.863	0.962	0.994	1.0	1.01	1.01	2.17	2.6
		^{31}P(p,α)^{28}Si	1.04	1.03	1.02	0.976	0.91	0.869	2.16	2.6
		^{41}Ca(n,α)^{38}Ar	0.964	0.968	0.984	1.02	1.1	1.15	2.2	2.6
		^{27}Al(α,n)^{30}P	0.878	0.973	0.997	1.0	1.0	1.0	2.17	2.65
		^{42}Ca(n,γ)^{43}Ca	1.14	1.11	1.04	0.961	0.91	0.895	2.17	2.6
		^{27}Al(α,γ)^{31}P	1.13	1.01	1.0	0.999	0.999	0.999	2.17	2.6
		^{43}Ca(n,γ)^{44}Ca	1.09	1.08	1.03	0.963	0.905	0.885	2.21	2.6
		^{47}Ca(n,γ)^{48}Ca	0.886	0.957	0.993	1.0	1.01	1.01	2.25	2.56
		^{45}Sc(p,α)^{42}Ca	0.887	0.983	0.998	1.0	1.0	1.0	2.17	2.6
		^{46}Sc(n,p)^{46}Ca	1.13	1.1	1.04	0.971	0.936	0.926	2.14	2.6
		^{16}O(^{12}C,p)^{27}Al	0.891	0.979	0.997	1.0	1.0	1.0	2.15	2.6
		^{28}Al(p,n)^{28}Si	1.01	1.01	1.0	0.994	0.964	0.891	2.21	2.6
		^{41}K(p,γ)^{42}Ca	1.12	1.04	1.01	0.997	0.994	0.993	2.2	2.6
		^{21}Ne(p,γ)^{22}Na	0.895	0.973	0.997	1.0	1.0	1.0	2.29	2.6
		^{41}K(n,γ)^{42}K	1.1	1.07	1.02	0.985	0.97	0.966	2.2	2.6
		^{30}P(n,p)^{30}Si	0.985	0.988	0.994	1.01	1.04	1.1	2.21	2.6
^{48}V (^{48}Cr)[a]	9.24e-05	^{48}Cr(α,p)^{51}Mn	0.395	0.572	0.834	1.2	1.84	3.13	1.83	3.57
		$\alpha(2\alpha,\gamma)^{12}$C	1.31	0.976	0.962	0.972	0.768	0.588	2.3	5.88
		^{12}C(α,γ)^{16}O	1.64	1.17	1.03	0.98	0.963	0.958	2.43	4.98
		^{44}Ti(α,p)^{47}V	1.2	1.16	1.06	0.932	0.766	0.629	1.1	4.33
		^{40}Ca(α,γ)^{44}Ti	1.15	1.12	1.05	0.941	0.793	0.664	2.16	2.84
		^{13}N(α,p)^{16}O	1.34	1.11	1.02	0.986	0.979	0.991	2.42	4.98
		^{47}V(p,γ)^{48}Cr	1.02	1.01	1.0	0.995	0.976	0.881	2.01	3.9
		^{42}Ca(α,γ)^{46}Ti	1.12	1.03	1.0	0.998	0.996	0.996	2.02	4.98
		^{16}O(^{12}C,p)^{27}Al	0.907	0.937	0.977	1.02	1.04	1.05	2.4	5.77
^{49}V	6.08e-06	^{12}C(α,γ)^{16}O	2.23	1.27	1.05	0.964	0.933	0.925	0.8	4.78
		^{49}Mn(p,γ)^{50}Fe	0.803	0.855	0.944	1.07	1.34	2.03	0.61	1.23
		^{49}V(p,γ)^{50}Cr	0.917	0.931	0.971	1.04	1.19	1.89	0.78	4.01
		^{49}Cr(n,p)^{49}V	0.705	0.797	0.933	1.07	1.25	1.49	0.7	3.9
		^{13}N(α,p)^{16}O	1.47	1.14	1.03	0.98	0.964	0.973	0.75	4.98
		^{44}Ti(α,p)^{47}V	1.02	0.994	0.991	1.02	1.12	1.44	0.8	4.1
		^{42}Ca(α,γ)^{46}Ti	1.3	1.07	1.01	0.995	0.99	0.989	0.74	4.49
		^{49}Cr(p,γ)^{50}Mn	0.813	0.875	0.958	1.04	1.12	1.17	0.62	1.21
		^{48}Cr(p,γ)^{49}Mn	1.15	1.12	1.04	0.955	0.87	0.82	0.58	1.03

Table 1 *continued*

Table 1 *(continued)*

Isotope	$X_{i,\text{rec}}$	Reaction	R_f For Reaction Rate Multiplied By:						T_9 Range	
			100	10	2	0.5	0.1	0.01	$T_{9,\text{low}}$	$T_{9,\text{high}}$
		$^{49}\text{Cr}(\alpha,\text{p})^{52}\text{Mn}$	0.826	0.96	0.995	1.0	1.01	1.01	0.7	3.73
		$^{20}\text{Ne}(\alpha,\gamma)^{24}\text{Mg}$	0.826	0.846	0.955	1.04	1.1	1.12	0.71	5.17
		$\alpha(2\alpha,\gamma)^{12}\text{C}$	1.1	0.93	0.95	1.01	0.932	0.833	0.58	6.13
		$^{48}\text{Cr}(\alpha,\text{p})^{51}\text{Mn}$	0.837	0.918	0.979	1.02	1.04	1.06	0.7	3.75
		$^{23}\text{Na}(\alpha,\text{p})^{26}\text{Mg}$	0.856	0.885	0.972	1.02	1.03	1.04	0.71	5.16
		$^{16}\text{O}(^{12}\text{C},\text{p})^{27}\text{Al}$	0.861	0.901	0.967	1.02	1.05	1.06	0.71	4.98
		$^{23}\text{Na}(\text{p},\gamma)^{24}\text{Mg}$	0.864	0.945	0.992	1.0	1.01	1.01	0.71	5.17
		$^{49}\text{Cr}(\text{n},\gamma)^{50}\text{Cr}$	0.867	0.98	0.998	1.0	1.0	1.0	0.71	3.69
		$^{16}\text{O}(^{12}\text{C},\alpha)^{24}\text{Mg}$	0.869	0.916	0.979	1.01	1.03	1.03	0.71	4.98
		$^{27}\text{Si}(\text{n},^{12}\text{C})^{16}\text{O}$	0.891	0.956	0.993	1.0	1.01	1.01	0.71	4.98
		$^{26}\text{Al}(\text{n},\alpha)^{23}\text{Na}$	0.899	0.949	0.992	1.0	1.01	1.01	0.72	5.17
		$^{50}\text{Mn}(\text{n},\text{p})^{50}\text{Cr}$	0.906	0.985	0.998	1.0	1.0	1.0	0.71	3.72
^{51}Cr	1.85e-05	$^{51}\text{Mn}(\text{p},\gamma)^{52}\text{Fe}$	0.306	0.569	0.848	1.18	1.74	3.13	0.96	3.09
		$^{48}\text{Cr}(\alpha,\text{p})^{51}\text{Mn}$	0.969	0.965	0.982	1.03	1.16	1.69	1.1	1.49
		$\alpha(2\alpha,\gamma)^{12}\text{C}$	0.948	0.9	0.955	0.999	0.869	0.724	0.73	5.85
		$^{27}\text{Al}(\alpha,\text{n})^{30}\text{P}$	1.37	1.1	1.01	0.993	0.988	0.986	0.87	1.98
		$^{44}\text{Ti}(\alpha,\text{p})^{47}\text{V}$	1.06	1.02	0.999	1.01	1.07	1.28	0.89	4.19
		$^{12}\text{C}(\alpha,\gamma)^{16}\text{O}$	1.28	1.11	1.02	0.971	0.963	0.961	0.85	4.98
		$^{42}\text{Ca}(\alpha,\gamma)^{46}\text{Ti}$	1.27	1.07	1.01	0.994	0.988	0.987	0.86	4.33
		$^{55}\text{Co}(\text{p},\gamma)^{56}\text{Ni}$	0.847	0.927	0.985	1.0	0.969	0.837	0.82	3.23
		$^{13}\text{N}(\alpha,\text{p})^{16}\text{O}$	1.17	1.06	1.02	0.986	0.976	0.988	0.84	5.17
		$^{33}\text{S}(\text{n},\alpha)^{30}\text{Si}$	1.15	1.05	1.01	0.997	0.995	0.994	0.85	1.93
		$^{53}\text{Fe}(\text{n},\text{p})^{53}\text{Mn}$	0.96	0.965	0.983	1.02	1.09	1.14	0.84	3.82
		$^{53}\text{Mn}(\text{p},\alpha)^{50}\text{Cr}$	0.878	0.97	0.996	1.0	1.0	1.0	0.82	3.71
		$^{20}\text{Ne}(\alpha,\gamma)^{24}\text{Mg}$	0.879	0.897	0.964	1.03	1.08	1.1	0.82	5.17
		$^{51}\text{Cr}(\text{p},\gamma)^{52}\text{Mn}$	0.987	0.989	0.996	1.01	1.03	1.12	0.84	3.81
		$^{50}\text{Cr}(\text{p},\gamma)^{51}\text{Mn}$	1.08	1.06	1.02	0.981	0.939	0.896	0.64	2.72
		$^{49}\text{Mn}(\text{p},\gamma)^{50}\text{Fe}$	1.02	1.01	1.0	0.998	1.03	1.12	0.8	1.38
		$^{45}\text{Sc}(\text{p},\alpha)^{42}\text{Ca}$	1.11	1.07	1.02	0.988	0.976	0.972	0.85	4.33
		$^{16}\text{O}(^{12}\text{C},\text{p})^{27}\text{Al}$	0.899	0.932	0.974	1.01	1.03	1.03	0.82	4.98
		$^{48}\text{Cr}(\text{p},\gamma)^{49}\text{Mn}$	1.02	1.02	1.01	0.987	0.949	0.903	0.69	1.16
		$^{54}\text{Fe}(\text{p},\gamma)^{55}\text{Co}$	1.0	1.0	1.0	0.998	0.982	0.904	0.82	2.58
		$^{16}\text{O}(^{12}\text{C},\alpha)^{24}\text{Mg}$	0.906	0.942	0.985	1.01	1.02	1.02	0.82	4.98
		$^{52}\text{Fe}(\alpha,\text{p})^{55}\text{Co}$	0.906	0.971	0.995	1.0	1.01	1.01	0.82	3.71
^{52}Mn	0.001	$^{12}\text{C}(\alpha,\gamma)^{16}\text{O}$	1.55	1.21	1.04	0.976	0.956	0.951	3.9	4.98
		$^{13}\text{N}(\alpha,\text{p})^{16}\text{O}$	1.39	1.15	1.03	0.979	0.953	0.941	3.9	4.98
		$^{52}\text{Fe}(\alpha,\text{p})^{55}\text{Co}$	0.732	0.871	0.962	1.04	1.15	1.27	2.72	3.63
		$^{44}\text{Ti}(\alpha,\text{p})^{47}\text{V}$	1.09	1.05	1.02	0.98	0.925	0.858	2.56	4.33
		$\alpha(2\alpha,\gamma)^{12}\text{C}$	1.11	0.856	0.917	0.993	0.918	0.863	2.27	5.98
		$^{53}\text{Fe}(\text{n},\text{p})^{53}\text{Mn}$	0.937	0.947	0.977	1.03	1.1	1.15	3.38	3.82
		$^{16}\text{O}(^{12}\text{C},\text{p})^{27}\text{Al}$	0.886	0.925	0.972	1.02	1.05	1.06	3.85	5.15
		$^{16}\text{O}(^{12}\text{C},\alpha)^{24}\text{Mg}$	0.897	0.935	0.981	1.01	1.03	1.03	3.85	4.98
		$^{53}\text{Mn}(\text{p},\alpha)^{50}\text{Cr}$	0.899	0.981	0.998	1.0	1.0	1.0	3.28	3.71
^{53}Mn	0.000107	$^{53}\text{Fe}(\text{n},\text{p})^{53}\text{Mn}$	0.546	0.707	0.902	1.1	1.3	1.42	2.93	3.72
		$^{12}\text{C}(\alpha,\gamma)^{16}\text{O}$	1.52	1.2	1.04	0.971	0.959	0.956	3.25	4.78
		$^{13}\text{N}(\alpha,\text{p})^{16}\text{O}$	1.36	1.14	1.03	0.975	0.943	0.931	3.21	4.78

Table 1 *continued*

Table 1 *(continued)*

Isotope	$X_{i,\text{rec}}$	Reaction	R_f For Reaction Rate Multiplied By:						T_9 Range	
			100	10	2	0.5	0.1	0.01	$T_{9,\text{low}}$	$T_{9,\text{high}}$
		^{52}Fe(p,γ)^{53}Co	1.23	1.09	1.02	0.987	0.969	0.961	0.74	1.01
		^{53}Mn(p,γ)^{54}Fe	0.956	0.976	0.992	1.01	1.04	1.19	3.15	3.81
		^{42}Ca(α,γ)^{46}Ti	1.15	1.05	1.01	0.995	0.991	0.99	3.56	4.49
		^{52}Fe(α,p)^{55}Co	0.87	0.949	0.988	1.01	1.03	1.05	2.8	3.63
		^{52}Fe(n,p)^{52}Mn	1.08	1.06	1.02	0.975	0.916	0.873	3.06	3.56
		^{16}O(^{12}C,p)^{27}Al	0.873	0.909	0.965	1.03	1.06	1.07	2.99	4.78
		^{16}O(^{12}C,α)^{24}Mg	0.881	0.921	0.977	1.01	1.03	1.03	2.98	4.98
		^{27}Si(n,^{12}C)^{16}O	0.9	0.954	0.993	1.0	1.01	1.01	2.99	4.78
		^{52}Mn(p,γ)^{53}Fe	1.0	1.0	1.0	0.997	0.983	0.906	3.06	3.62
		^{53}Fe(n,γ)^{54}Fe	0.907	0.989	0.999	1.0	1.0	1.0	3.05	3.56
^{55}Fe	0.000495	^{55}Co(p,γ)^{56}Ni	0.605	0.761	0.921	1.09	1.32	1.8	2.21	3.13
		^{12}C(α,γ)^{16}O	1.53	1.23	1.05	0.96	0.939	0.932	3.81	5.17
		^{13}N(α,p)^{16}O	1.39	1.15	1.04	0.97	0.929	0.907	3.9	5.6
		^{16}O(^{12}C,p)^{27}Al	0.858	0.893	0.957	1.03	1.06	1.07	3.57	5.15
		^{16}O(^{12}C,α)^{24}Mg	0.864	0.907	0.972	1.02	1.03	1.04	3.58	4.49
		^{42}Ca(α,γ)^{46}Ti	1.15	1.05	1.01	0.995	0.99	0.989	3.56	4.49
		^{12}C(^{12}C,α)^{20}Ne	1.14	1.09	1.02	0.984	0.967	0.963	3.19	5.17
		^{12}C(^{12}C,p)^{23}Na	1.14	1.07	1.02	0.989	0.978	0.975	3.36	5.17
		^{27}Si(n,^{12}C)^{16}O	0.886	0.946	0.992	1.0	1.01	1.01	3.65	4.49
		^{23}Na(α,p)^{26}Mg	0.887	0.894	0.965	1.02	1.04	1.04	3.54	5.16
		^{54}Fe(p,γ)^{55}Co	1.0	1.0	1.0	1.0	1.02	1.12	2.37	2.83
^{56}Co (^{56}Ni)[a]	0.0875	α(2α,γ)^{12}C	1.24	1.14	1.05	0.944	0.847	0.803	3.22	5.77
		^{12}C(α,γ)^{16}O	1.11	1.04	1.01	0.996	0.993	0.992	3.99	4.98
^{57}Co (^{57}Ni)[a]	0.00256	^{57}Ni(n,p)^{57}Co	0.727	0.809	0.934	1.07	1.24	1.38	2.04	3.48
		α(2α,γ)^{12}C	1.1	1.1	1.02	0.978	0.915	0.87	2.55	5.55
		^{56}Ni(p,γ)^{57}Cu	1.14	1.03	1.01	0.996	0.991	0.989	0.46	0.64
		^{27}Al(α,n)^{30}P	1.11	1.03	1.0	0.998	0.996	0.995	2.64	3.22
		^{57}Ni(n,γ)^{58}Ni	0.907	0.986	0.998	1.0	1.0	1.0	2.93	3.31
^{59}Fe	3.92e-05	^{59}Fe(n,γ)^{60}Fe	0.687	0.843	0.967	1.02	1.04	1.04	1.32	2.34
		^{58}Fe(n,γ)^{59}Fe	1.31	1.15	1.04	0.964	0.903	0.871	1.32	2.34
		^{24}Mg(n,γ)^{25}Mg	0.825	0.859	0.946	1.05	1.12	1.14	1.32	2.34
		^{25}Mg(α,n)^{28}Si	1.21	1.15	1.05	0.966	0.93	0.921	1.34	2.34
		^{20}Ne(α,γ)^{24}Mg	0.832	0.879	0.962	1.03	1.07	1.08	1.32	2.34
		^{20}Ne(n,γ)^{21}Ne	0.844	0.918	0.983	1.01	1.02	1.02	1.32	2.34
		^{16}O(α,γ)^{20}Ne	1.07	1.06	1.03	0.965	0.891	0.849	1.32	2.34
		^{25}Mg(n,γ)^{26}Mg	0.853	0.905	0.974	1.02	1.04	1.05	1.32	2.34
		^{59}Fe(p,n)^{59}Co	0.858	0.96	0.994	1.0	1.01	1.01	1.32	2.34
		^{25}Mg(p,γ)^{26}Al	0.871	0.918	0.98	1.01	1.03	1.03	1.32	2.34
		^{28}Al(p,α)^{25}Mg	1.13	1.06	1.01	0.994	0.989	0.988	1.34	2.38
		^{28}Si(n,γ)^{29}Si	0.888	0.962	0.993	1.0	1.01	1.01	1.32	2.34
		^{26}Mg(α,n)^{29}Si	1.12	1.08	1.03	0.974	0.937	0.925	1.34	2.34
		^{27}Al(α,p)^{30}Si	0.907	0.951	0.988	1.01	1.02	1.02	1.32	2.34
		^{58}Fe(p,γ)^{59}Co	0.908	0.97	0.995	1.0	1.01	1.01	1.32	2.34
^{59}Ni	0.000162	^{59}Cu(p,γ)^{60}Zn	0.274	0.464	0.775	1.29	2.12	2.77	1.37	2.39
		^{57}Cu(p,γ)^{58}Zn	1.68	1.17	1.02	0.989	0.982	0.974	0.78	1.07
		^{59}Cu(p,α)^{56}Ni	1.41	1.25	1.06	0.963	0.93	0.963	1.25	2.39

Table 1 *continued*

Table 1 *(continued)*

Isotope	$X_{i,\mathrm{rec}}$	Reaction	R_f For Reaction Rate Multiplied By:						T_9 Range	
			100	10	2	0.5	0.1	0.01	$T_{9,\mathrm{low}}$	$T_{9,\mathrm{high}}$
		$^{57}\mathrm{Ni}(n,p)^{57}\mathrm{Co}$	0.856	0.894	0.955	1.06	1.21	1.39	1.19	2.96
		$\alpha(2\alpha,\gamma)^{12}\mathrm{C}$	0.739	0.893	0.964	1.01	0.924	0.847	1.08	5.72
		$^{20}\mathrm{Ne}(\alpha,\gamma)^{24}\mathrm{Mg}$	0.937	0.948	0.98	1.03	1.13	1.31	1.73	2.04
		$^{57}\mathrm{Ni}(p,\gamma)^{58}\mathrm{Cu}$	1.01	1.01	1.0	0.989	0.926	0.788	1.21	1.6
		$^{27}\mathrm{Al}(\alpha,n)^{30}\mathrm{P}$	1.25	1.06	1.01	0.995	0.994	1.0	1.19	1.54
		$^{48}\mathrm{Cr}(\alpha,p)^{51}\mathrm{Mn}$	0.974	0.979	0.993	1.01	1.08	1.22	1.18	1.51
		$^{58}\mathrm{Ni}(p,\gamma)^{59}\mathrm{Cu}$	1.02	1.01	1.0	0.997	0.961	0.849	1.29	2.4
		$^{30}\mathrm{Si}(p,\gamma)^{31}\mathrm{P}$	0.981	0.978	0.992	1.01	1.08	1.14	1.37	2.6
		$^{33}\mathrm{S}(n,\alpha)^{30}\mathrm{Si}$	1.14	1.04	1.0	1.0	0.999	1.0	1.27	1.96
		$^{58}\mathrm{Cu}(p,\gamma)^{59}\mathrm{Zn}$	1.0	1.0	1.0	1.01	0.972	0.882	1.24	1.63
		$^{26}\mathrm{Al}(n,\alpha)^{23}\mathrm{Na}$	1.13	1.03	1.0	1.0	0.996	0.994	1.18	1.92
		$^{58}\mathrm{Ni}(\alpha,\gamma)^{62}\mathrm{Zn}$	0.905	0.973	0.993	0.997	1.01	1.01	1.27	2.65

[a] Sensitivity of long-lived parent isotope is the same

REFERENCES

Banerjee, P., Qian, Y.-Z., Heger, A., & Haxton, W. C. 2016, Nature Communications, 7, 13639

Beard, M., Austin, S., & Cyburt, R. 2017, Phys. Rev. Lett., 119, 112701

Benyamin, D., & Shaviv, N. J. 2018, ApJ, 863, 86

Boggs, S. E., Harrison, F. A., Miyasaka, H., et al. 2015, Science, 348, 670

Borkowski, K. J., Reynolds, S. P., Green, D. A., et al. 2010, The Astrophysical Journal, 724, L161

Burrows, A., Reddy, S., & Thompson, T. A. 2006, Nuclear Physics A, 777, 356 , special Issue on Nuclear Astrophysics

Chieffi, A., & Limongi, M. 2017, The Astrophysical Journal, 836, 79

Clayton, D. D. 2011, The Role of Radioactive Isotopes in Astrophysics, ed. R. Diehl, D. H. Hartmann, & N. Prantzos, Vol. 812, 25–82

Cook, W. R., Palmer, D. M., Prince, T. A., et al. 1988, ApJL, 334, L87

Côté, B., Lugaro, M., Reifarth, R., et al. 2019, ApJ, 878, 156

Couch, S. M., Warren, M. L., & O'Connor, E. P. 2020, ApJ, 890, 127

Curtis, S., Ebinger, K., Fröhlich, C., et al. 2019, ApJ, 870, 2

Cyburt, R. H., Amthor, A. M., Ferguson, R., et al. 2010, The Astrophysical Journal Supplement Series, 189, 240

Diehl, R. 2016, Journal of Physics: Conference Series, 665, 012011

Diehl, R. 2017, in American Institute of Physics Conference Series, Vol. 1852, 040004

Dufour, F., & Kaspi, V. M. 2013, The Astrophysical Journal, 775, 52

DuVernois, M. A. 1997, The Astrophysical Journal, 481, 241

Fields, C. E., Timmes, F. X., Farmer, R., et al. 2018, The Astrophysical Journal Supplement Series, 234, 19

Fuller, G. M., Fowler, W. A., & Newman, M. J. 1985, ApJ, 293, 1

Grebenev, S. A., Lutovinov, A. A., Tsygankov, S. S., & Winkler, C. 2012, Nature, 490, 373 EP

Grefenstette, B. W., Harrison, F. A., Boggs, S. E., et al. 2014, Nature, 506, 339

Hix, W. R., & Thielemann, F.-K. 1996, ApJ, 460, 869

Hoffman, R. D., Woosley, S. E., Weaver, T. A., Rauscher, T., & Thielemann, F. K. 1999, ApJ, 521, 735

Hoffman, R. D., Sheets, S. A., Burke, J. T., et al. 2010, ApJ, 715, 1383

Hoppe, P., Strebel, R., Eberhardt, P., Amari, S., & Lewis, R. S. 1996, Science, 272, 1314

Hunter, J. D. 2007, Computing in Science and Engineering, 9, 90

Iliadis, C., Champagne, A., Jose, J., Starrfield, S., & Tupper, P. 2002, The Astrophysical Journal Supplement Series, 142, 105

Israel, M., Binns, W., Cummings, A., et al. 2005, Nuclear Physics A, 758, 201 , nuclei in the Cosmos VIII

Iyudin, A. F., Diehl, R., Bloemen, H., et al. 1994, A&A, 284, L1

Jerkstrand, A., Fransson, C., & Kozma, C. 2011, A&A, 530, A45

Jordan, G. C., Gupta, S. S., & Meyer, B. S. 2003, Phys. Rev. C, 68, 065801

Kurfess, J. D., Johnson, W. N., Kinzer, R. L., et al. 1992, ApJL, 399, L137

Langanke, K., & Martínez-Pinedo, G. 2000, Nuclear Physics A, 673, 481

Leising, M. 2006, New Astronomy Reviews, 50, 557 , astronomy with Radioactivities. V

Leising, M. D. 2001, The Astrophysical Journal, 563, 185

Lippuner, J., & Roberts, L. F. 2017, The Astrophysical Journal Supplement Series, 233, 18

Lugaro, M., Ott, U., & Kereszturi, Á. 2018, Progress in Particle and Nuclear Physics, 102, 1

Magkotsios, G., Timmes, F. X., Hungerford, A. L., et al. 2010, ApJS, 191, 66

Mahoney, W. A., Varnell, L. S., Jacobson, A. S., et al. 1988, ApJL, 334, L81

Marek, A., Dimmelmeier, H., Janka, H.-T., Müller, E., & Buras, R. 2006, A&A, 445, 273

Matz, S. M., Share, G. H., Leising, M. D., et al. 1988, Nature, 331, 416

McKinney, W., et al. 2010, in Proceedings of the 9th Python in Science Conference, Vol. 445, Austin, TX, 51–56

Meyer, B. S., & Clayton, D. D. 2000, Space Science Reviews, 92, 133

Meyer, B. S., Krishnan, T. D., & Clayton, D. D. 1998, ApJ, 498, 808

Neronov, A., & Meynet, G. 2016, A&A, 588, A86

Nittler, L. R., Amari, S., Zinner, E., Woosley, S. E., & Lewis, R. S. 1996, ApJL, 462, L31

Nittler, L. R., & Ciesla, F. 2016, Annual Review of Astronomy and Astrophysics, 54, 53

Nomoto, K., Tominaga, N., Umeda, H., Kobayashi, C., & Maeda, K. 2006, Nuclear Physics A, 777, 424 , special Isseu on Nuclear Astrophysics

O'Connor, E. 2015, ApJS, 219, 24

Oda, T., Hino, M., Muto, K., Takahara, M., & Sato, K. 1994, Atomic Data and Nuclear Data Tables, 56, 231

Paxton, B., Marchant, P., Schwab, J., et al. 2015, The Astrophysical Journal Supplement Series, 220, 15

Rauscher, T., Heger, A., Hoffman, R. D., & Woosley, S. E. 2002, ApJ, 576, 323

Renaud, M., Vink, J., Decourchelle, A., et al. 2006, ApJL, 647, L41

Sallaska, A. L., Iliadis, C., Champange, A. E., et al. 2013, The Astrophysical Journal Supplement Series, 207, 18

Sandie, W. G., Nakano, G. H., Chase, Jr., L. F., et al. 1988, ApJL, 334, L91

Sawada, R., & Maeda, K. 2019, arXiv e-prints, arXiv:1910.06972

Scott, L. M. 2005, PhD thesis, Washigton University, St. Louis, Missouri, USA

Seitenzahl, I. R., Timmes, F. X., & Magkotsios, G. 2014, ApJ, 792, 10

Siegert, T., Diehl, R., Krause, M. G. H., & Greiner, J. 2015, A&A, 579, A124

Steiner, A. W., Hempel, M., & Fischer, T. 2013, ApJ, 774, 17

Stephan, T., Trappitsch, R., Davis, A. M., et al. 2016, International Journal of Mass Spectrometry, 407, 1

Sukhbold, T., Ertl, T., Woosley, S., Brown, J. M., & Janka, H.-T. 2016, The Astrophysical Journal, 821, 38

Takigawa, A., Miki, J., Tachibana, S., et al. 2008, The Astrophysical Journal, 688, 1382

Teegarden, B. J., Barthelmy, S. D., Gehrels, N., et al. 1989, Nature, 339, 122

The, L. S., Clayton, D. D., Jin, L., & Meyer, B. S. 1998, ApJ, 504, 500

The, L. S., Clayton, D. D., Diehl, R., et al. 2006, A&A, 450, 1037

Timmes, F., Fryer, C., Timmes, F., et al. 2019, BAAS, 51, 2

Tissot, F. L., Dauphas, N., & Grove, T. L. 2017, Geochimica et Cosmochimica Acta, 213, 593

Tuli, J. K. 2011, Nuclear Wallet Cards 2001, 8th Edition

Tur, C., Heger, A., & Austin, S. M. 2010, ApJ, 718, 357

van der Walt, S., Colbert, S. C., & Varoquaux, G. 2011, Computing in Science and Engineering, 13, 22

Vance, G. S., Young, P. A., Fryer, C. L., & Ellinger, C. I. 2020, The Astrophysical Journal, 895, 82

Vink, J. 2005, Advances in Space Research, 35, 976 , young Neutron Stars and Supernova Remnants

Vink, J., Laming, J. M., Kaastra, J. S., et al. 2001, ApJL, 560, L79

Warren, M. L., Couch, S. M., O'Connor, E. P., & Morozova, V. 2019, arXiv preprint arXiv:1912.03328

Wasserburg, G., Busso, M., Gallino, R., & Nollett, K. 2006, Nuclear Physics A, 777, 5 , special Isseu on Nuclear Astrophysics

Wheeler, J. C., Maund, J. R., & Couch, S. M. 2008, The Astrophysical Journal, 677, 1091

Wiedenbeck, M. E., Binns, W. R., Christian, E. R., et al. 1999, The Astrophysical Journal, 523, L61

Witti, J., Janka, H. T., & Takahashi, K. 1994, A&A, 286, 841

Woosley, S., & Heger, A. 2007, Physics Reports, 442, 269 , the Hans Bethe Centennial Volume 1906-2006

Woosley, S. E., & Heger, A. 2015, ApJ, 810, 34

Woosley, S. E., Heger, A., & Weaver, T. A. 2002, Reviews of Modern Physics, 74, 1015

Woosley, S. E., & Hoffman, R. D. 1992, ApJ, 395, 202

Woosley, S. E., & Weaver, T. A. 1995, ApJS, 101, 181

Young, P. A., Fryer, C. L., Hungerford, A., et al. 2006, ApJ, 640, 891

Zimmerman, W. R., Ahmed, M. W., Bromberger, B., et al. 2013, Phys. Rev. Lett., 110, 152502